
Article:
Chinembiri, K., He, S. orcid.org/0000-0003-0326-2447, Li, J. et al. (1 more author) (2021) Natural circulation in a short-enclosed rod bundle. International Journal of Heat and Mass Transfer, 179. 121674. ISSN 0017-9310

https://doi.org/10.1016/j.ijheatmasstransfer.2021.121674

Natural circulation in a short-enclosed rod bundle

Kenneth Chinembiri[a], Shuisheng He[a,*], Jiankang Li[b], Cosimo Trinca[a]

[a]*Heat, Flow and Turbulence Research Group, Department of Mechanical Engineering, The University of Sheffield, S1 3JD, UK*

[b]*Fuel Route Systems Branch, Engineering, EDF Energy Generation, Barnett Way, Barnwood, Gloucester, GL4 3RS, UK*

Abstract

Large Eddy Simulation (LES) is used to study natural circulation flow in a sealed rod bundle with a Rayleigh number (based on height) of approximately 10^{11} and a fluid Prandtl number of 0.74. Natural convection boundary layer development is observed on both the heating rods and cooling containment surfaces. The development of the boundary layers is key to the flow and heat transfer characteristics of the system. As the flow descends on the containment surface, the boundary layer gradually develops and transitions from laminar to turbulent flow, with transition occurring close to the bottom-end. Laminar flow at the containment is well represented by a flat plate similarity solution for buoyant flow and the Nusselt number correlation is akin to that for a flat isolated vertical surface. This indicates the boundary layer development on this surface is similar to an isolated vertical surface. On the rods boundary layer development occurs much earlier and is affected by turbulence convected from the containment surface. Laminar flow here compares well against a slender cylinder similarity solution. In the developed region, the Nusselt number correlation has a Rayleigh number dependency similar to that for a rectangular cavity.

Keywords: Natural circulation, LES, Rod bundle, Heat transfer

1. Introduction

Natural convection is prevalent in a large number of industrial systems. Examples within the nuclear industry include integrated passive safety systems, irradiated fuel storage ponds and storage casks. Such systems comprise of components with complicated geometric configurations. One, for example, can imagine rod bundle arrays within the fuel bun-

* s.he@sheffield.ac.uk

dle or the multiple serpentine tube rows in a boiler unit.

Natural convective flow has been the subject of intensive research in the past. However, this has been mostly limited to simple geometries such as rectangular or annular cavities. For more complex configurations, there is a distinct lack of literature. Studies presented in the forthcoming literature review mostly pertain to simple cavities, but the flows are nonetheless complex and of relevance to the present study.

Elder[1, 2] was among the first investigators to report experimental results for laminar and turbulent natural convection in a vertical-cavity at multiple aspect ratios. Up to $\mathrm{Ra}_L = 10^7$, the growth and formation of "travelling-like-waves" fronts on both the hot and cold surfaces were observed. Increasing Ra_L further leads to these waves growing, forming "hook" like structures and becoming increasingly unstable. This eventually leads to turbulent transition as the "hook" like structures break off, instigating strong and violent mixing between the core and boundary layer. Elder[2] further states boundary layer development on the surfaces is akin to that for flat vertical plates. Macgregor and Emery[3] noted several flow regimes from their numerical and experimental data. The conduction regime at $\mathrm{Ra}_L \leq 10^3$, which was characterised by a linear temperature profile across the cavity. In the next regime "asymptotic flow" at $10^3 < \mathrm{Ra}_L < 10^4$, both conduction and convection contribute to heat transfer. This regime would then transition to a "laminar boundary layer flow" regime at $10^4 < \mathrm{Ra}_L < 10^6$. Where convection dominates with the flow constrained to the wall layers. The core is quiescent and has a uniform temperature. At Rayleigh numbers between $10^6 < \mathrm{Ra}_L < 10^7$ the flow is considered transitional. After $\mathrm{Ra}_L = 10^7$ the flow would then transition to the turbulent boundary layer flow regime.

Nomenclature

Greek letters

α	thermal diffusivity, $\lambda/\rho\mathrm{Cp}\,[m^2/s]$
β	thermal expansion coefficient, $1/(T+273.15)\,[1/^\circ\mathrm{C}]$
ΔT	Horizontal temperature difference (unless stated otherwise)
ΔT_V	Vertical temperature difference
δ_{ij}	Kronecker delta
λ	thermal conductivity, [W/m$^\circ$C]

μ	molecular viscosity,[Pa s]
ρ	density, $\left[kg/m^3\right]$

Roman Letters

A	aspect ratio, H/L
Cf	Fanning friction factor, $\tau_w/\rho\left(w^2/2\right)$
Cp	specific heat capacity, [J/kg°C]
$\mathrm{Gr}_{\Delta T}$	Grashof number, $g\beta\left(T_w-T\right)L^3/(v^2)$
$\mathrm{Gr}_{q''}$	Grashof number, $g\beta q''L^4/(v^2\lambda)$
H	Height,[m]
Nu	Nusselt number, hL/λ
Pr	Prandtl number, μCp/λ
Ra	Rayleigh number, GrPr
D	diameter, [m]
g	gravity, $\left[m/s^2\right]$
h	heat transfer coefficient, $\left[\mathrm{W}/\left(\mathrm{m}^2\,^\circ\mathrm{C}\right)\right]$
k	turbulent kinetic energy, $\left[m^2/s^2\right]$
L	length scale, [m]
p/d	pitch-to-diameter ratio
q''	heat flux,$\left[\mathrm{W}/\mathrm{m}^2\right]$
R	radius, [m]
r	radial distance,[m]
T	temperature,[°C]
t	time, [s]
T^*	non-dimensional temperature
u,v,w	velocity components,[m/s]
V	reference velocity,[m/s]
v	kinematic viscosity,$\mu/\rho\left[\mathrm{m}^2/\mathrm{s}\right]$
x,y,z	spatial distances, [m]
Z^*	non-dimensional height

Subscripts

c	cold surface
crs	cross flow
h	hot surface
i,j,k	directional terms
max	maximum velocity
$num-diff$	numerical diffusion
sgs	subgrid scale
w	wall

Turbulent natural convection in a tall cavity of aspect ratio (A) 28.6 was investigated by Betts and Bokhari[4]. Temperature differentials of 19.6°C and 39.69°C were considered giving Rayleigh numbers $\left(\mathrm{Ra}_L\right)$ of 0.86×10^6

and 1.43×10^6, respectively. Mean and turbulent quantities were measured in the experiment to provide validation data for turbulence models.

The hot and cold boundary layer flows interacted with each other leading to a turbulent core with peak velocity fluctuations occurring here. At half-height, there was a linear velocity and temperature gradient across the core. This is in contrast to results from the smaller aspect ratio cavities, where the core has a uniform temperature and is stagnant[2, 3].

Lewandowski et al.[5] experimentally investigated natural convection in a symmetrically heated vertical channel. Multiple aspect ratios ranging from 2.8 to 11 were investigated. It was shown that the gap spacing had a significant influence on the flow and heat transfer. In the study air was the working fluid with a given Prandtl number of 0.71 and a peak Rayleigh number (Ra_H) of 10^9.

Laminar natural convection in a rectangular cavity was numerically and analytically investigated by Kimura and Bejan[6]. The aspect ratios considered ranged from 1 to 3. Their results showed the boundary layer thickness was constant in the laminar boundary layer regime. Linear stratification and a motionless core were predicted at $\mathrm{Gr}_L = 5 \times 10^5$ and A = 2.

The physical mechanisms for the temporal and spatial onset of transition in rectangular cavities were investigated using DNS simulations by Paolucci and Chenoweth[7]. At the critical Rayleigh number, turbulence transition was a result of instabilities in the vertical boundary layer. However at aspect ratios $0.5 < \mathrm{A} < 3$, internal waves near the departing corners lead to transition. Departing corners were defined as where the flow is ejected to the interior cavity from the side wall boundary layers. At significant Rayleigh numbers (much larger than the critical value), then both transition instabilities can be present.

Nakao et al.[8] numerically investigated natural convection boundary layer development on a heated vertical wall. In their study, the LES method with a modified Smagorinsky model was used. Numerical results obtained compared well with experimental data for the laminar and turbulent regions. The onset and duration of the transition regime were found to vary with the streamwise grid resolution to some extent. Profiles for the Reynolds stresses were shown to peak on the outer layer.

Versteegh and Nieuwstadt[9] used DNS to simulate natural convection in an infinite differentially heated rectangular vertical channel.

Temperature and velocity profiles showed they could be split into two regions; one (near the wall) where the viscous effects are dominant and the second region in-between the velocity maxima and core where the turbulence effects dominate. Turbulence budgets showed, transport due to advection was of importance only near the velocity maximum. In the near-wall region, it was shown the turbulent shear stress at higher Rayleigh numbers tended to become negative. Paolucci[10] simulated a rectangular cavity using DNS and also showed that near the wall the turbulent shear stress was negative.

Goodrich and Marcum[11] experimentally studied the effect of the radius of curvature on flow transition and heat transfer. Five cylindrical heating rods with diameters ranging from 0.0064 m to 0.025 m were considered by the authors. Results showed that at large values of Ra_D the influence of curvature was nearly negligible with the heat transfer being approximated by flat plate correlations.

Keyhani et al.[12] conducted experimental investigations for laminar and turbulent natural convection in square rod bundle arrays. Two-rod bundle arrangements for a 5 x 5 and 3 x 3 array, with given pitch-to-diameter (p/d) ratios of 2.25 and 3.08, respectively were investigated. A flow visualisation study was carried out for the 3 x 3 bundle study. Boundary layer flow was observed on the rod surfaces. The sub-channel centres were largely stagnant and regions of low magnitude downward flow. Nusselt number correlations for air and helium were obtained for the separate rod bundle configurations. For the 5 x 5 bundle their Nusselt number correlation in the boundary layer flow regime was $0.095\mathrm{Ra}_D^{0.323}$ for helium. The correlations for the 3 x 3 rod bundle were $0.072\mathrm{Ra}_D^{0.332}$ in helium/air and $0.151\mathrm{Ra}_D^{0.274}$ in water. The Rayleigh number was defined using the outer cylinder diameter with Rayleigh number limits of $2.6\times10^5 \leq \mathrm{Ra}_D \leq 1.06\times10^9$ and $1.2\times10^5 \leq \mathrm{Ra}_D \leq 4.5\times10^7$ for the 5 x 5 and 3 x 3 rod bundle Nusselt correlations, respectively. However, the paper has little to no discussion on the flow or turbulence analysis. In a subsequent paper, Keyhani and Dalton[13] experimentally study natural convection in a horizontally oriented rod bundle. From this study and others[14, 15], it is shown that the flow in horizontal rods significantly differs from that of vertically oriented arrays.

Arshad et al.[16] experimentally investigated turbulent natural convection in water for an isolated vertical thin rod and a 3 x 3 array consisting of such rods. High Rayleigh

numbers were considered and the derived correlation was $0.325\mathrm{Ra}_H^{0.24}$ for the central rod. This correlation is valid between $1.28 \times 10^{12} \leq \mathrm{Ra}_H \leq 1.18 \times 10^{13}$. Khalifa and Hussein[17] similarly investigate natural convection in a 3 x 3 array but with heating only applied to three of the rods. The correlation for the inner most rod was $0.0049\mathrm{Ra}_H^{0.3485}$. Similar to Keyhani et al.[12], these papers[16, 17] focused on heat transfer and provided no information on the flow and turbulence.

A numerical investigation for laminar natural convection in a sub-channel of a seven-rod bundle array was carried out by Rao and Glakpe[18] for Rayleigh numbers ranging from 10^2 to 10^8. Predictions at low Rayleigh numbers showed the flow was in the pseudo-conduction regime and had no bearing on the temperature distribution. At higher Rayleigh numbers thermal stratification was the result of strong boundary layer flow.

The brief literature review above shows a lack of literature on natural convection in enclosed rod bundles at high Rayleigh numbers detailing flow, thermal development and turbulence structures. This paper aims to add to this body of knowledge by conducting Large Eddy Simulations of natural circulation flow in a sealed rod bundle. The geometry investigated herein is of relatively low aspect ratio, with a value based on the height and the largest distance between the heating rods to containment wall of 3.5. A parallel study has been conducted for a large aspect ratio cavity with a corresponding value of 14[19]. The flow there is dominated by strong circulation and turbulence, whereas herein the flow is characterised by stagnation in the core and a laminar boundary layer development followed by transition at the walls.

Section 2 describes the numerical setup, governing equations and the problem setup. Results for the solved variables, energy spectrum, turbulence structures, statistics, heat transfer and friction factor correlations are presented in Section 3. Finally, the concluding remarks are presented in Section 4.

2. Computational Methodology

2.1. Governing Equations

LES simulations are carried out using the CFD solver Code_Saturne. The solver is an open-source, finite volume and single-phase code developed by EDF[20]. In LES, the filtered incompressible Navier-Stokes equations, presented below, are numerically solved for:

Continuity:

$$\frac{\partial \rho}{\partial t} + \frac{\partial \rho \overline{u_i}}{\partial x_i} = 0 \tag{1}$$

Momentum:

$$\begin{aligned} \frac{\partial \rho \overline{u_i}}{\partial t} + \frac{\partial}{\partial x_j}\left(\rho \overline{u_i}\,\overline{u_j}\right) &= -\frac{\partial \overline{P}}{\partial x_i} + \rho g_i \\ &+ \mu \frac{\partial}{\partial x_j}\left(\frac{\partial \overline{u_i}}{\partial x_j} + \frac{\partial \overline{u_j}}{\partial x_i}\right) - \frac{\partial \rho \tau_{ij}^r}{\partial x_j} \end{aligned} \tag{2}$$

Energy:

$$\rho\left(\frac{\partial \overline{T}}{\partial t} + \frac{\partial \overline{u_i}\,\overline{T}}{\partial x_i}\right) = \frac{\mu}{\mathrm{Pr}} \frac{\partial^2 \overline{T}}{\partial x_i x_i} - \frac{\partial \rho \Pi_{\mathrm{sgs},i}}{\partial x_i} \tag{3}$$

The equations presented above (1 to 3) are spatially filtered. Filtering the momentum equation leaves it open and the term τ_{ij}^r, which represents the residual stress needs to be modelled. This can be done using the eddy viscosity assumption as shown in Equation 4.

$$\tau_{ij}^r = -2 v_{\mathrm{sgs}} \overline{S_{ij}} + \frac{1}{3}\tau_{kk}\delta_{ij} \tag{4}$$

Where $\overline{S_{ij}}$ is defined as $\frac{1}{2}\left(\frac{\partial \overline{u_i}}{\partial x_j} + \frac{\partial \overline{u_j}}{\partial x_i}\right)$. In the energy equation, the term Π is computed using the subgrid viscosity and turbulent Prandtl number:

$$\Pi_{\mathrm{sgs},i} = \frac{v_{\mathrm{sgs}}}{\mathrm{Pr}_t} \frac{\partial \overline{T}}{\partial x_i} \tag{5}$$

The open terms are treated as follows; $\frac{1}{3}\tau_{kk}\delta_{ij}$ is treated by defining a modified pressure (i.e. $\overline{P^*} = \overline{P} + \frac{1}{3}\tau_{kk}\delta_{ij}$), while the turbulent Prandtl number (Pr_t) is defined as a fixed constant.

In the present simulations, the subgrid viscosity is computed using the Wall Adapting Local Eddy viscosity (WALE) subgrid model by Nicoud and Ducros[21] and is defined as:

$$v_{\mathrm{sgs}} = (\mathrm{C_m} \cdot \Delta)^2 \frac{\left(\overline{S_{ij}^d}\,\overline{S_{ij}^d}\right)^{3/2}}{\left(\overline{S_{ij}}\,\overline{S_{ij}}\right)^{5/2} + \left(\overline{S_{ij}^d}\,\overline{S_{ij}^d}\right)^{5/4}} \tag{6}$$

where $\overline{S_{ij}^d}$ is defined as $\frac{1}{2}\left(\left(\frac{\partial \overline{u_i}}{\partial x_j}\right)^2 + \left(\frac{\partial \overline{u_j}}{\partial x_i}\right)^2\right) - \frac{1}{3}\delta_{ij}\left(\frac{\partial \overline{u_i}}{\partial x_j}\right)^2$. Δ is the grid size, which is computed as $(\Delta x \cdot \Delta y \cdot \Delta z)^{1/3}$. Finally, $\mathrm{C_m}$ is a model constant and in Code_Saturne is taken to be 0.25.

2.2. Geometry

The heating rods are arranged in a similar pattern to that found in an Advanced Gas Reactor (AGR) fuel bundle. Figure 1 gives an illustration of the rod arrangement. The height of the modelled rod bundle is however shortened to a quarter giving a height of 0.25 m. The rod and containment diameters are 0.0153 m and 0.1923 m, respectively. The central rod termed the "guide tube" is a non-heating sur-

face. Heating is applied at the three concentric ranks of fuel rods. Their radial locations are defined as 0.025 m, 0.051 m and 0.079 m giving an approximate p/d ratio of 1.8.

At this stage, it is worth defining the aspect ratios of the modelled domain. Typically in cavities, the characteristic length is defined as the distance between the hot and cold surfaces. In this geometry, as there are three concentric ranks of heated rods, thus three aspect ratios can be defined. With aspect ratio defined as H/L where H is the height and L is the radial distance between the centroid of the heated rod and containment wall, the computed values are 3.5, 5.5, 14.3 going from the first to the third-rank.

2.3. Properties, boundary conditions and numerical setup

The coolant is carbon dioxide at a pressure of 3 MPa. Density variation as a function of temperature is modelled with a lookup table using data obtained from the National Institute of Standards and Technology (NIST) database[22]. All the remaining physical properties are fixed constants and the values used are given in Table 1.

The fuel rod surfaces are considered smooth, with a constant heat flux applied. Two heat fluxes of 289 W/m^2 and 1154 W/m^2 are considered in this study. At the containment surface, a convective boundary condition is applied, with a sink temperature of 110 °C and a heat transfer coefficient of 700 W/m^2 °C. The azimuthal surfaces (edge surfaces for a 60°C sector) are assigned rotational periodicity boundary conditions. All the surfaces are considered no-slip. The central rod (guide tube), top and bottom walls are considered adiabatic.

Table 1: Physical property constants imposed on the fluid

Property	Value	Units
Dynamic viscosity	2.712×10^{-5}	Pa s
Thermal conductivity	0.04	W/m°C
Specific heat	1088	J/kg°C
Prandtl number	0.737	-

Table 2: Case definition

Case name	Heat flux
Case-1	1154W/m^2
Case-2	289 W/m^2

The second-order accurate Second Order Linear Upwind (SOLU) scheme is used for spatial discretisation, while temporal discretisation uses the second-order Crank-Nicholson scheme.

The LES simulations are initialised from a converged URANS (Unsteady Reynolds Averaged Navier-Stokes) solution. Initialising from URANS results ensures a much faster convergence. Statistical averaging of the LES computation is carried out after the mean variables (taken from probes located at the rod gaps) have converged. Typically, statistical averaging is carried out for over a 100 s simulated time. The simulation is judged to have converged once the time variations of the mean profiles (velocity, temperature and turbulent kinetic energy) are small.

2.4. Non-dimensional parameters and Mesh quality statistics

Non-dimensional parameters are presented for the cases in Table 3. The Rayleigh number is computed using both the temperature and heat flux definitions. The definitions used for the Rayleigh number are given in Equation 7:

$$\mathrm{Ra}_{\Delta T_V} = \frac{g\beta\Delta T_V L^3}{\nu\alpha} \tag{7a}$$

$$\mathrm{Ra}_{q''} = \frac{g\beta q''_w L^4}{\nu\alpha\lambda} \tag{7b}$$

Since the width of the rod bundle cavity can be considered dependent on the rod ranks; two values are given for the first rank (Ra_{L-1}) and third rank (Ra_{L-3}) rods as they represent the upper and lower limit, respectively. Additionally, it is also possible to define the Rayleigh number based on the height of the domain.

Table 3: Rayleigh numbers for the heating cases considered using different length scales.

Parameter	Case-1	Case-2
$\mathrm{Ra}_{H,\Delta T_V}$	1.9×10^{11}	1.1×10^{11}
$\mathrm{Ra}_{L-1,\Delta T_V}$	4.3×10^{9}	2.4×10^{9}
$\mathrm{Ra}_{L-3,\Delta T_V}$	6.4×10^{7}	3.6×10^{7}
$\mathrm{Ra}_{H,q''}$	6.8×10^{12}	3.3×10^{12}
$\mathrm{Ra}_{L-1,q''}$	4.5×10^{10}	2.2×10^{10}
$\mathrm{Ra}_{L-3,q''}$	1.6×10^{8}	7.9×10^{7}

A fully structured mesh consisting of 25 million elements, shown in Figure 1, is used. The first near-wall adjacent nodes have a y^+ value range of $0.0053 \leq y^+ \leq 0.33$, with grid spacing values of $\Delta x^+ = 30.0$ and $\Delta z^+ = 36$ in the span-wise and stream-wise directions, respectively. These values are calculated for the highest heating case at mid-height.

The mesh aspect ratio values are highest in the boundary layer (occurring at the first cell layer with an overall peak value of 36). Away from the walls, the aspect ratio decreases, and is between 1 to 1.8 for the the majority of the cells in the core. For the constricted cells across the second rank rod, the majority of the cells are below 6. Higher aspect ratios typi-

cally occur close to the walls due to the wall-normal grid requirements. However, the flow is aligned with the cells thus the impact on accuracy or convergence is limited.

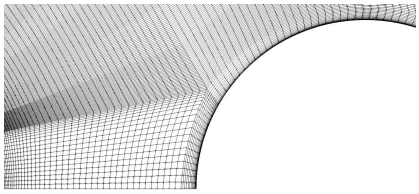

(a)

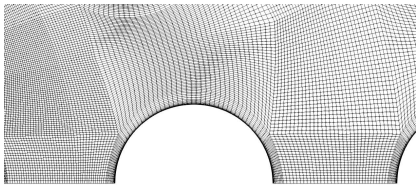

(b)

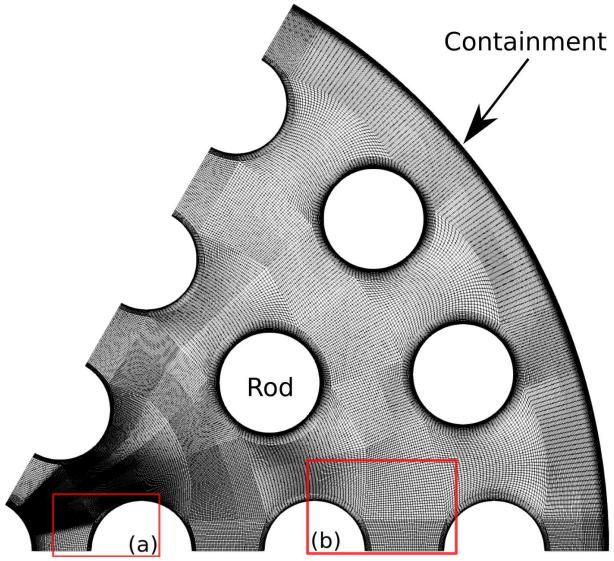

(c) Full cross-sectional figure

Fig. 1: Cross-sectional resolution of the mesh used in the LES computations.

A fixed time step of 0.0002 s is maintained for the highest heating case, while for the lower heating case the time step is doubled to 0.0004 s. The Courant number predominantly ranges from nearly 0 (stagnant sub-channel core) to 0.5. It should be noted that for the highest heating case there is a peak transient fluctuation albeit very brief where the maximum Courant number is approximately 1 before suddenly reducing. However, this does occur in only several cells $<<<$ 1%.

To assess the time step in terms of flow physics the viscous time scale around the containment surface is defined as:

$$\Delta t = \frac{\nu}{\overline{w}_\tau^2} \tag{8}$$

The computed wall time step based on the LES simulation data is shown in Figure A1. The lowest time step is approximately 7.5×10^{-4}. This demonstrates the time step used is very conservative and is limited only by the numerical stability.

To assess the convergence of the simulation profiles were plotted at varying intervals. Figure 2 shows the time convergence of the highest heating case (Case-1) extracted across Line_1 and Line_5 (see Figure 3 for extraction locations). The profiles plotted over a 30 s duration and reveal there is little variation indicating a well-converged result. To determine the quality of the mesh used for the LES simu-

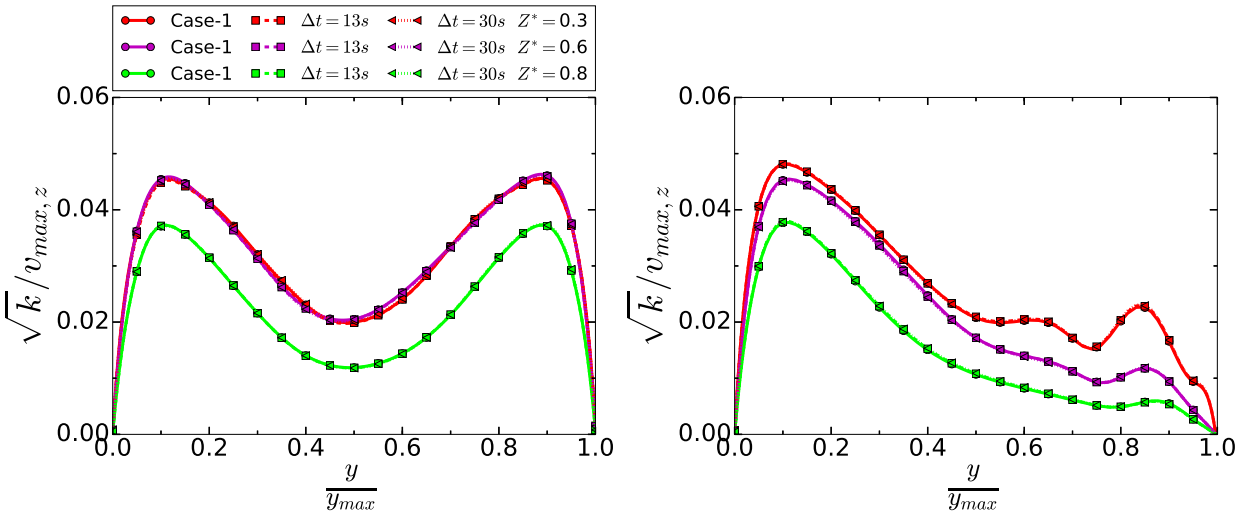

(a) Line_1 (b) Line_5

Fig. 2: Profiles of a time convergence study for turbulent kinetic energy variation taken along Line_1 and Line_5 (see Figure 3 for extraction locations). The reference velocity $v_{max,z}$ is the peak axial velocity extracted at profile height.

lation, the quality parameter, LES_IQ$_v$, by Celik et al.[23] is used. The quality parameter (LES_IQ$_v$) is defined as shown in Equation 9.

$$\text{LES\_IQ}_v = \frac{1}{1+0.05\left(\frac{S^*}{1-S^*}\right)^{0.53}} \qquad (9)$$

S^* is computed as shown in Equation 10. Where it has been taken the subgrid scale diffusion is equal to the numerical diffusion $\left(\mu_{\text{sgs}} \approx \mu_{\text{num-diff}}\right)$.

$$S^* = \frac{\mu_{\text{sgs}} + \mu_{\text{num-diff}}}{\mu_{\text{sgs}} + \mu_{\text{num-diff}} + \mu} \qquad (10)$$

The meshes used for the LES computations are considered to be good if this value is above 80%. Computing this parameter gives minimum values of 0.92 and 0.94 LES_IQ$_v$ for case-1 and case-2, respectively. These values indicate the LES simulations are of overall good quality. Contour plots of LES_IQ$_v$ are shown in Figure A2.

3. Results

3.1. A qualitative overview of the general flow behaviour

Qualitative data presented in this section is predominantly obtained from the highest heating case (Case-1) unless stated otherwise. To aid in the identification of data extraction points Figure 3 is included.

Vertical contour plots are presented in Figure 4 for Case-1 and are taken at $\theta = 30°$.

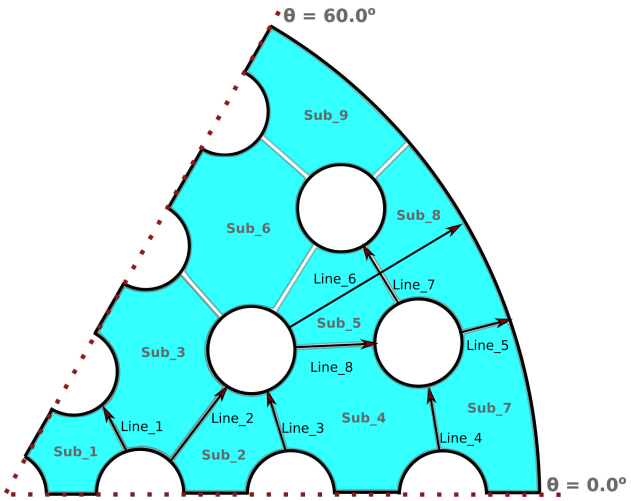

Fig. 3: Schematic showing the sub-channel divisions (denoted by Sub_*). Also included are the lines used to extract the profiles, with the start $(y/y_{max} = 0)$ and end point $(y/y_{max} = 1)$ given by the direction of the arrow.

Where applicable, the velocity scales are normalised using the buoyant velocity $V_{n,\Delta T_V}$, which is defined as $(g\beta\Delta T\nu)^{1/3}$. Cross slices taken at varying axial locations are shown in Figures 5 to 6. Variables in the cross slices are normalised using the local quantities at the extracted location.

It can be seen from Figure 4 that the flow is largely constrained to the boundary layers. Significant upward and downward flow occurs near the rod and containment surfaces, respectively. However, the core is nearly stagnant with some hints of low magnitude downward flow. Keyhani et al.[12] made similar observations in his experimental work. At the containment wall, boundary layer development can be seen starting from an initially stagnant top-end. The boundary layer thickness grows as the flow descends. Cross-flows are shown to be significant at the ends of the domain (Figure 5) with the bottom-end showing greater vector magnitudes. Based on the cross-flow magnitudes and the large observed regions of stagnant flow there appears to be no-interaction between neighbouring rods (except near the domain ends). Thus it can be further stated; away from the domain ends the rods essentially behave as if they are isolated. The flow regime qualitatively evidenced thus far is akin to a boundary layer flow regime.

Peak turbulence levels occur at the containment surface near the bottom-end of the domain see Figures 4(c) and 6(a). For the fuel pins, it is apparent turbulent kinetic energy peaks near the wall, which is synonymous with shear flows. For the containment surface, there is no turbulence at the top of the domain but high levels at the bottom end. Coupled with the observed axial velocity contours, it is evident there is a natural convection boundary layer forming on this surface, which is initially laminar but transition to a turbulent state occurs near the bottom-end. This will be discussed further later. Development to a fully turbulent core as observed for example

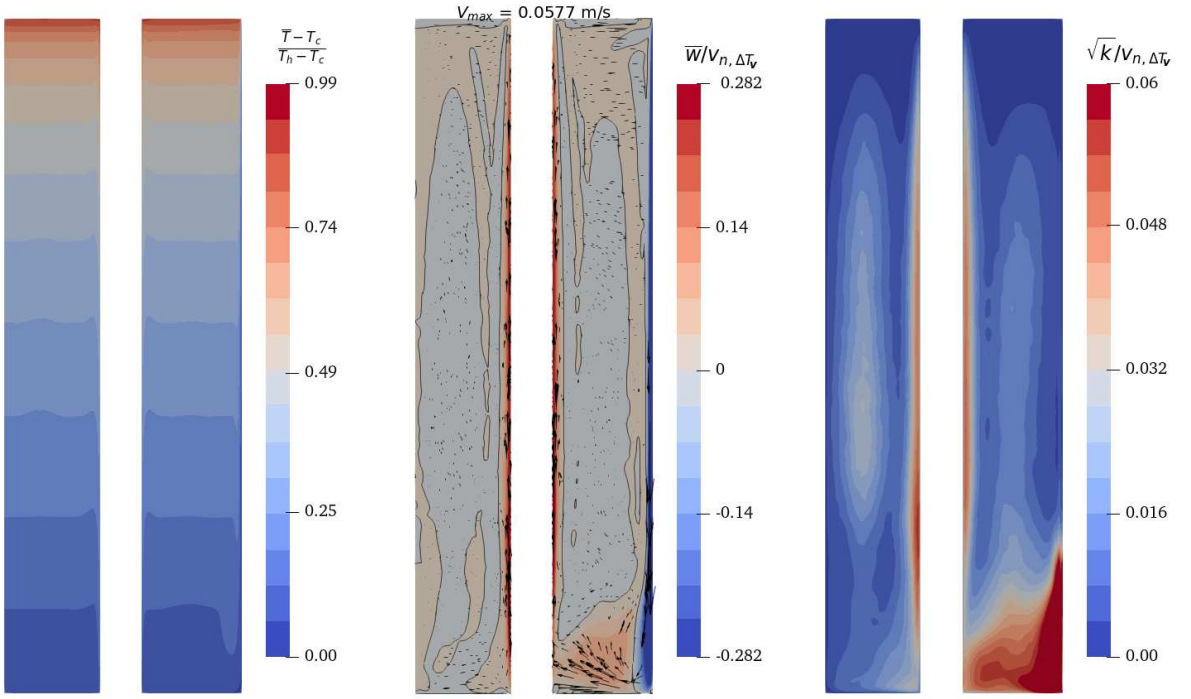

(a) Normalised temperature

(b) Normalised velocity

(c) Normalised turbulence kinetic energy

Fig. 4: Contours of temperature, velocity and turbulent kinetic energy taken from Case-1. Slices are taken at $\theta = 30°$. Velocity and turbulent kinetic energy are normalised using the buoyant velocity ($V_{n,\Delta T_V}$). The black contour line (only shown for velocity) is specified at $\overline{w}/V_{\max,z} = 0.0$.

in Elder's[2] or Betts and Bokhari's[4] work is impeded by the short nature of the modelled domain.

Enhanced turbulence levels can be observed on the rods away from the top and bottom-ends. Unlike the containment wall, there is a rapid development to a turbulent state. It is worth noting, the turbulence peaks are again located near the walls. Figure 4(c) shows at approximately mid-height, the core region has slightly elevated turbulence levels. Cross slices for velocity have shown the boundary layers are thicker at mid-height (Figure 5(b)). Turbulent kinetic energy (Figure 6(c) at the rod gaps (easily seen for first rank rods) is enhanced compared to the levels observed at the sub-channel cores. Noting that Figure 4(c) is taken from a plane at $\theta = 30°$, it is clear the local enhanced core regions (away from the heated surfaces and transition region) are a result of the surrounding rods at either side of the plane.

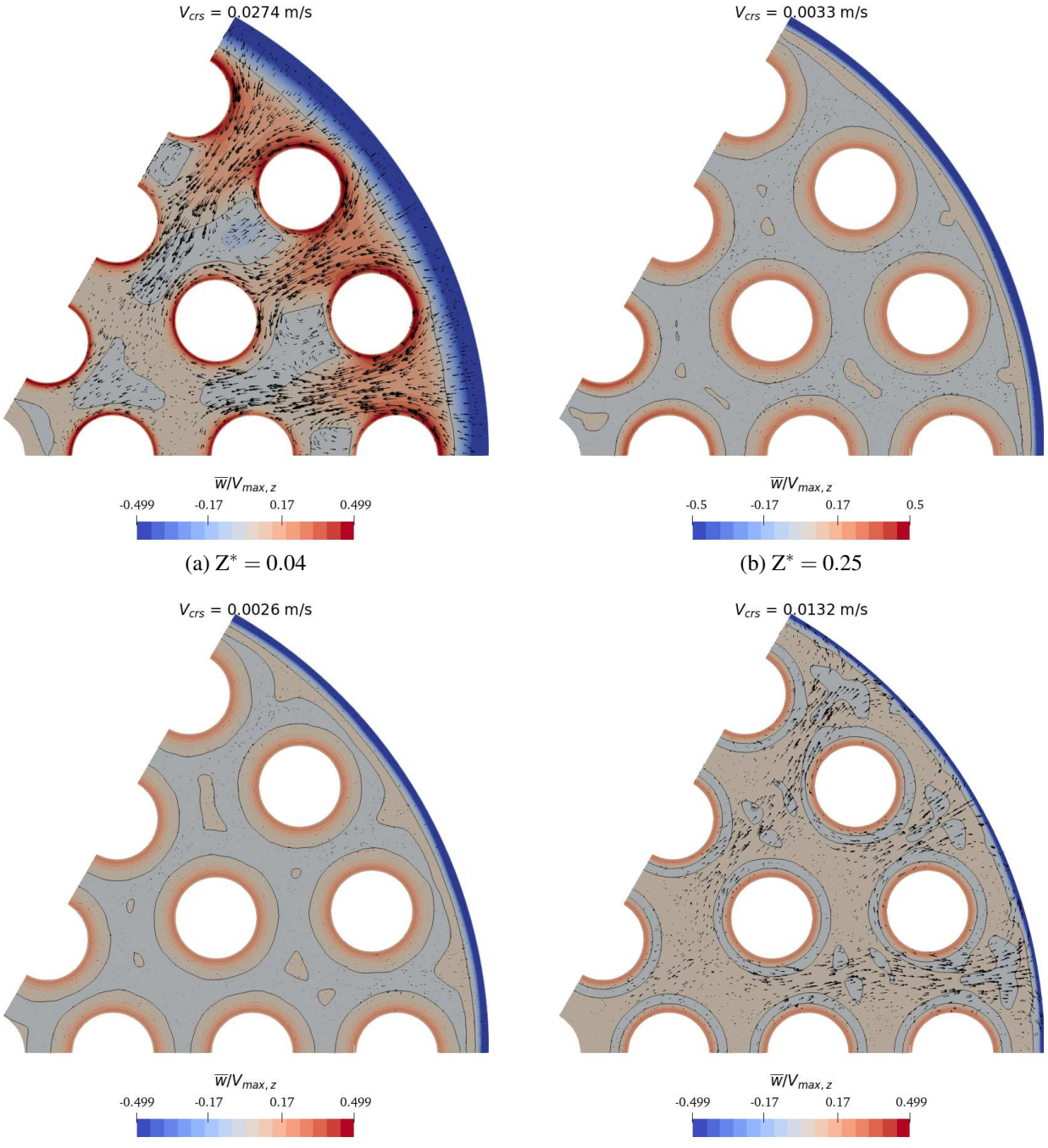

(a) $Z^* = 0.04$ (b) $Z^* = 0.25$

(c) $Z^* = 0.5$ (d) $Z^* = 0.96$

Fig. 5: Contours of the axial velocity extracted from Case-1 and taken at varying heights. The black contour line is specified at $\overline{w}/V_{\max,z} = 0.0$. Where $V_{\max,z}$ is the peak axial velocity of the slice. The cross-flow vector peak (V_{crs}) is given in each sub-figure and the value is dimensional.

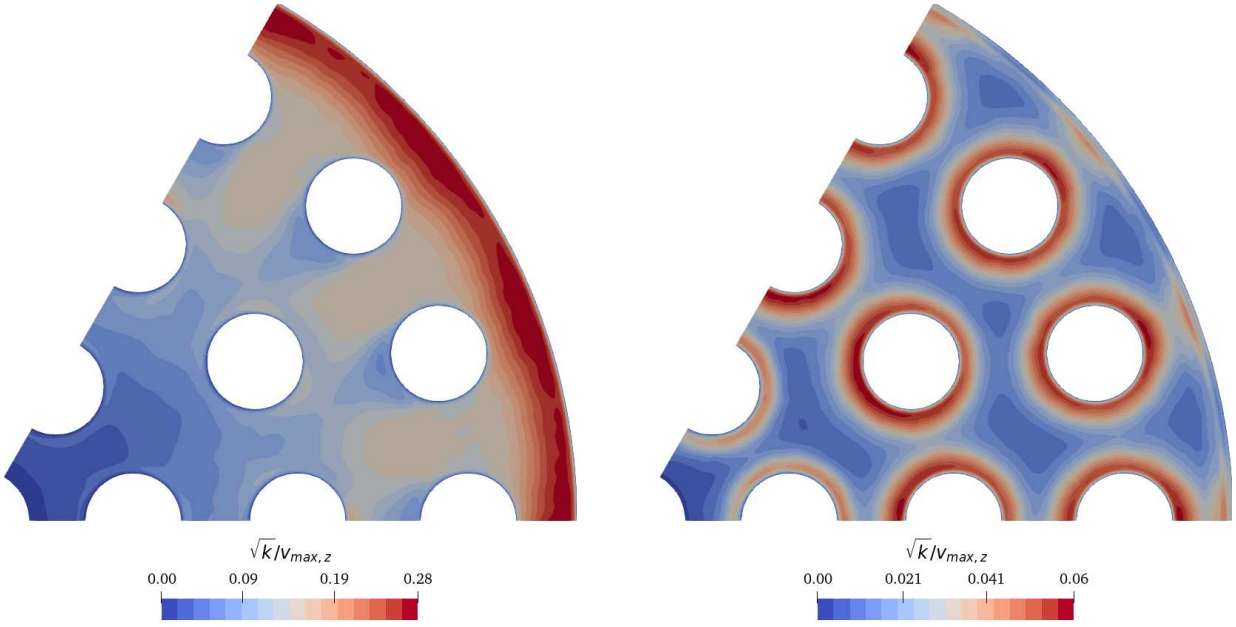

(a) $Z^* = 0.04$ (b) $Z^* = 0.25$

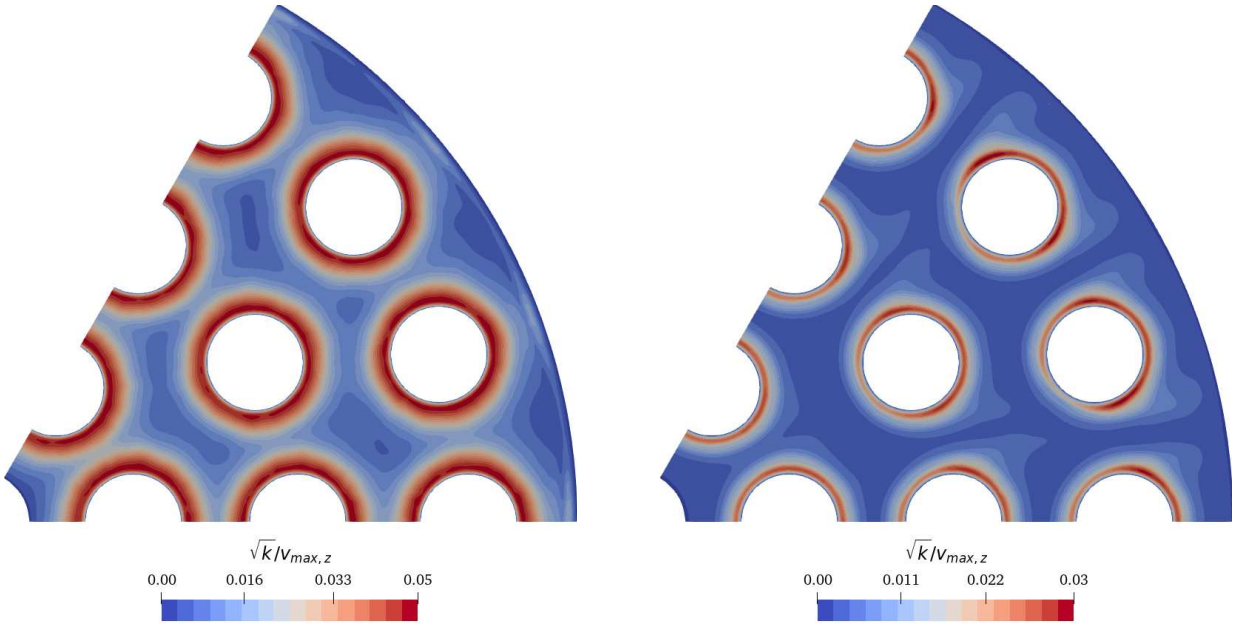

(c) $Z^* = 0.5$ (d) $Z^* = 0.96$

Fig. 6: Contours of turbulent kinetic energy extracted from Case-1 and taken at varying heights. The scalebar is reset at each axial location to maximise the variation. The contours are normalised using the peak velocity of the slice.

Vertical temperature plots (Figure 4 (a)) clearly show a stratified core. The core is shown to be a region of uniform temperature with horizontal temperature variation occurring close to the walls (across the thin boundary layers).

Iso-surfaces computed using Q-criterion and then coloured with the instantaneous streamwise vorticity are shown in Figure 7. The streamwise vorticity is coloured at ± 30. As can be seen, there is intense activity along the rod walls with the structures disappearing close to the top surface. The most intense activity is noted near the bottom containment wall. Figure 7(b) initially shows a spanwise vortex rollup along the containment surface. Descending further downwards it is followed by numerous pairs of counter-rotating coherent structures. In the core no structures are evident.

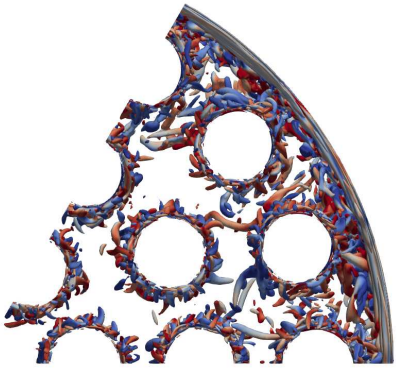

(a) Top down view

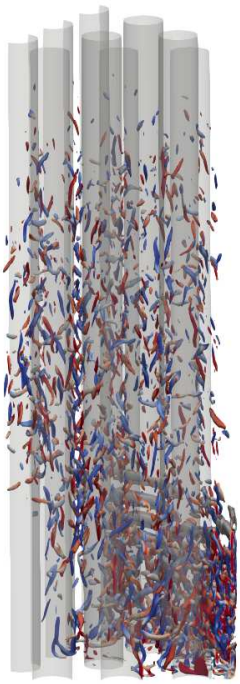

(b) Oblique view

Fig. 7: Iso-surfaces coloured by the streamwise vorticity. Data is taken from the Case-1.

3.2. Quantitative analysis

Figure 8 shows plots for the axial velocity extracted across different lines and heights for the cases under consideration. In each of the sub-plots, black-thin lines are superimposed and represent the profile computed at mid-height. To aid in showing flow development, velocity profiles are normalised using a constant buoyant velocity. Additional profiles close to the bottom and top wall are presented in Figures 9 and 10, respectively.

Profiles in Figure 8 clearly show a, nearly, stagnant core at all data extraction points. Flow is constrained to the near-wall regions.

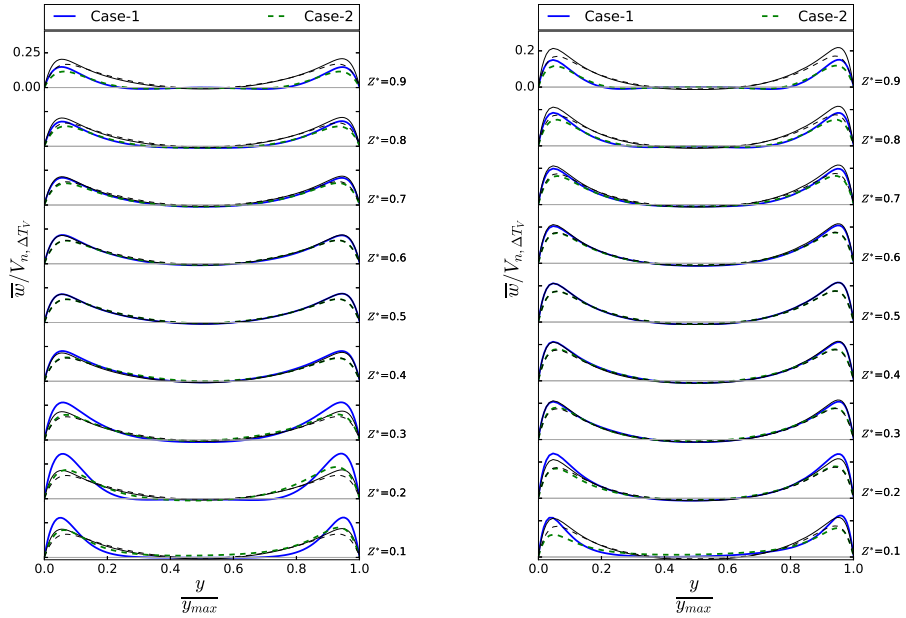

(a) Line_1 (b) Line_3

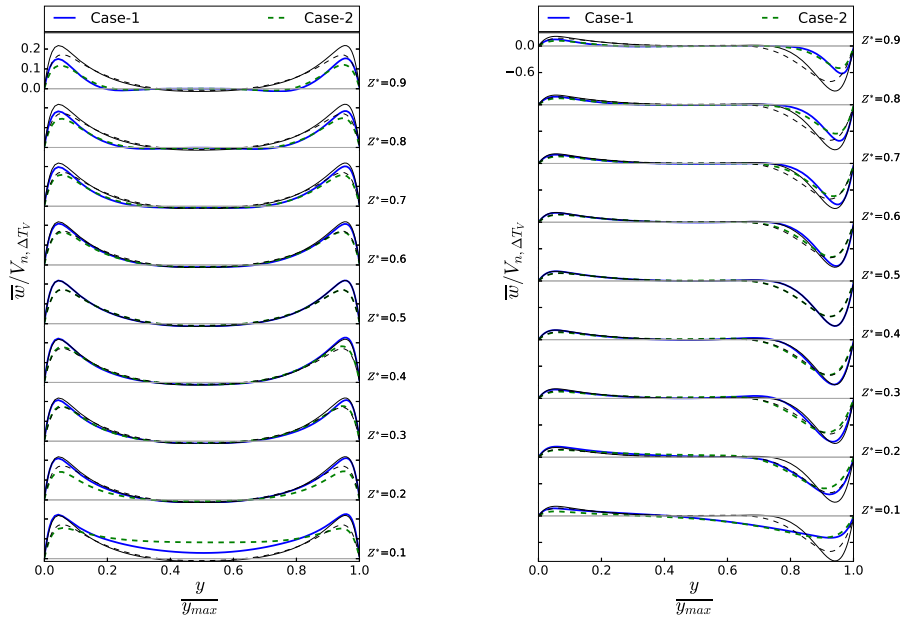

(c) Line_4 (d) Line_5

Fig. 8: Axial velocity profiles plotted at different axial locations. To show flow development the profiles are normalised using the buoyancy velocity $\left(V_{n,\Delta T_V} = (g\beta\Delta T_V \nu)^{1/3}\right)$. The superimposed black-thin lines are for the profiles taken at mid-height $Z^* = 0.5$ for the cavity. Line styles for the mid-height profiles are follow those given for the case. The scale for each respective sub-figure is shown in the upper left corner.

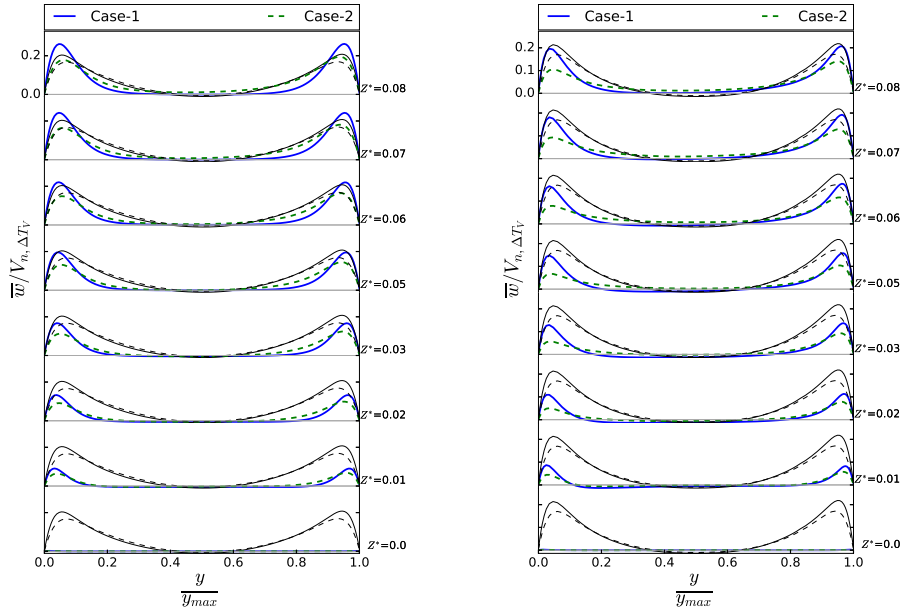

(a) Line_1 (b) Line_3

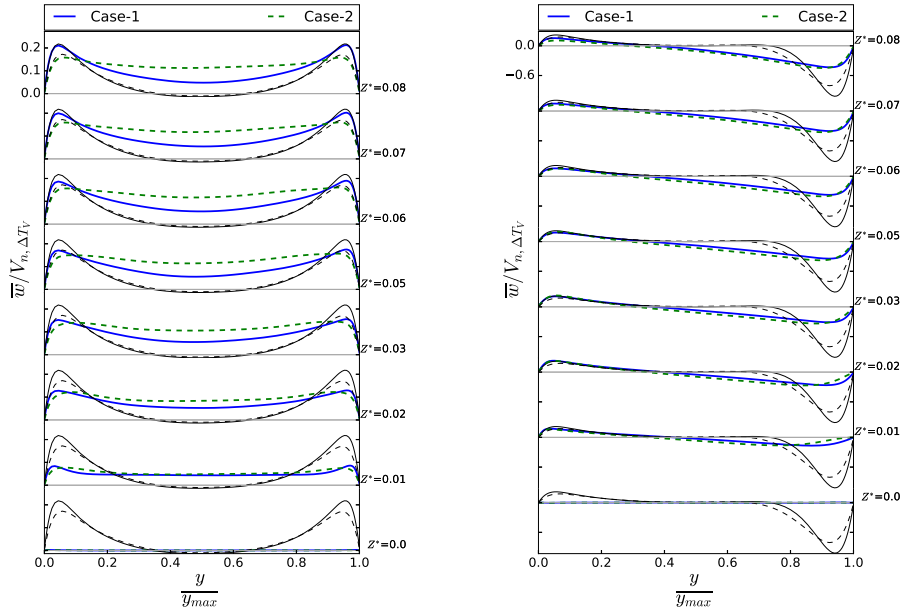

(c) Line_4 (d) Line_5

Fig. 9: Axial velocity profiles plotted near the bottom wall. At heights inetween $Z^* = 0.0$ to 0.08. To show flow development, the profiles are normalised using the buoyant velocity $\left(V_{n,\Delta T_V} = (g\beta\Delta T_V \nu)^{1/3}\right)$. The superimposed black-thin lines are for the profiles taken at mid-height for the cavity. Line styles for the mid-height profiles follow that given for the case. The scale for each respective sub-figure is shown in the upper left corner.

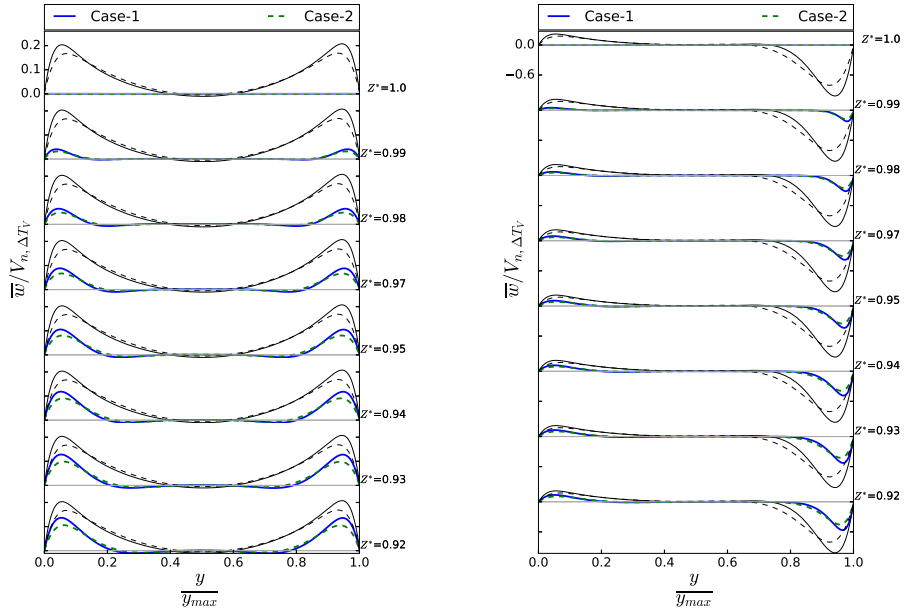

(a) Line_1 (b) Line_5

Fig. 10: Axial velocity profiles plotted near top wall taken at a height $Z^* = 0.92$ to 1.0. To show flow development, the profiles are normalised using the buoyany velocity $\left(V_{n,\Delta T_V} = (g\beta\Delta T_V \nu)^{1/3}\right)$. The superimposed black-thin lines are for the profiles taken at mid-height for the cavity. Line styles for the mid-height profiles follow that given for the case. The scale for each respective sub-figure is shown in the upper left corner.

Sub-figures 8 (a, b & c) are taken across the rod gaps and their behaviours are similar. Consider Case 1 along Line_1 for example (Figures 9(a) and 10(a)). The flow boundary layer is formed on the rod surface at the bottom of the domain, which grows in terms of both the boundary layer thickness and the peak velocity with the height until around Z^* = 0.2. The peak then reduces and the boundary layer thickness broadens. Later we will see that the flow is laminar initially and transition occurs around $Z^* \approx 0.1$. Largely, between $Z^* \approx 0.3$ or 0.4 and 0.7, the profiles at the gaps are effectively identical and retain the peak velocity. Past $Z^* = 0.7$, the flow starts to decelerate as the end effects of the confined domain gradually increase in influence. Close inspection reveals Line_1, Line_3, and Line_4 show different flow development lengths. These lines are extracted across the rod gaps and are at varying proximity to the containment wall. Line_1 extracted for the first rank rods starts to retain the mid-height velocity profile at $Z^* = 0.4$ and shows signs of departure (profiles start changing in comparison to mid-height profile) at $Z^* \approx 0.7$. Sim-

ilarly, Line_3 and Line_4 depart at $Z^* = 0.7$, but fully develop earlier at $Z^* = 0.3$. Interestingly, at $Z^* = 0.1$ and below, Line_4 has a net upward flow through the rod gap. At this location, the flow behaves almost like a heated vertical pipe. Line_1 and Line_3, largely exhibit a typical buoyancy driven boundary layer development. While the initial development for Line_4 is almost akin to forced/mixed convection flow (see Figure9 (c)) before transitioning to the more typical buoyancy driven flow past $Z^* = 0.1$. Differences in the flow development can be attributed to the spread of turbulence after the containment surface transitions. As seen in Figure 4(b&c) strong turbulence generation occurs here along with a strong entrainment and ejection of the flow between the containment wall and interior sub-channels. Turbulence transition on the containment is further discussed later. The rod gap profiles after a development interval, fully develop and stop evolving until the flow approaches the top-end $(Z^* \approx 0.7)$. This behaviour is worth discussing: Assuming an isolated vertical plate with a constant heat flux applied at the heating wall, it is expected the boundary layer would grow with vertical distance. The far field temperature is fixed to that of the quiescent region and this would be invariant with height. While, the wall temperature increases with height, consequently so does the buoyancy force. However, in the current geometry the flow is constrained. The far field temperature is associated with that of the sub-channel cores and as demonstrated in Figure 4(a) varies with height. The retention of the profiles once the flow is developed strongly indicates the temperature difference between the wall and core is largely maintained. This implies, within this developed region the vertical temperature gradient of the wall and core are largely the same.

The flow development along the containment shows a similar trend as well, but the flow is from top to bottom as fluid is cooled here. Also, significantly different is that there is no overshoot of the velocity profile development. The boundary layer develops between $Z^* = 1$ down to around $Z^* = 0.6$, after which the profile remains largely unchanged until $Z^* = 0.3$. From here the velocity reduces as the flow goes toward the bottom wall. It will be shown later, turbulence transition occurs a lot later on this wall at around $Z^* = 0.3$. Comparing, the different cases it can be noted typically at most locations, Case-1 has the peak velocity.

Temperature profiles are presented in Figure

11 between $Z^* = 0.1$ and $Z^* = 0.9$. Profiles close to the top and bottom ends are presented in Figure 12. To normalise, the peak wall temperature $T_{h,z}$ and minimum temperature $T_{c,z}$ of the profile are used. The rod gap profiles between $Z^* = 0.1$ upto $Z^* = 0.9$ largely do not show significant variation. For, Line_1 similarity is reached at $Z^* = 0.2$ and maintained until $Z^* = 0.7$. In comparison, for velocity development is reached at $Z^* \approx 0.33$. It is interesting to note, temperature reaches similarity much sooner than velocity does for the rod gaps and the thermal boundary layer thickness is largely maintained. However, near the containment surface, the temperature development closely mirrors the observations made for velocity. Using Line_5 as an example, temperature profiles develop (from top to bottom) reaching similarity at $Z^* = 0.6$ with the profiles remaining unchanged until $Z^* = 0.33$.

Temperature profiles at the top and bottom ends are given in Figure 12. At the containment surface, the temperature differential is largest at the top-end as the hot gas begins its descent. Looking at Figure 12(b) the temperature gradient at the containment surface decreases as distance increases from the top surface.

At the bottom-end for the rod gaps, the relative temperature differential is typically steeper than at mid-height. Cold gas arriving from the containment wall approaches the heated rods and ascends, which would explain the steeper gradient. Temperature inversion occurs at the top-end of the domain between $Z^* = 0.9$ to $Z^* = 0.99$. As height increases, the inversion progressively worsens. Right at the top wall $Z^* = 1.0$ a parabolic temperature profile is observed. As seen from Figure 10, here the axial velocity has stagnated even at the boundary layers and this would help explain the drastic shift from the temperature inversion profile.

Turbulent kinetic energy is shown in Figure 13. Normalization is carried out using the peak velocity of the profile. Figure 14 shows the profiles close to the bottom-end of the domain. These profiles in Figure 14 are normalised using the buoyant velocity. It is necessary to use the buoyant velocity as close to the domain ends, the computed peak velocity is nearly zero.

Turbulence peaks largely occur near the wall as expected. At the top, the flow tends to laminarize with no turbulent kinetic energy levels at $Z^* = 1.0$ (profiles are not shown). This is largely due to the flow stagnating at this region. On the containment wall (Line_5), tur-

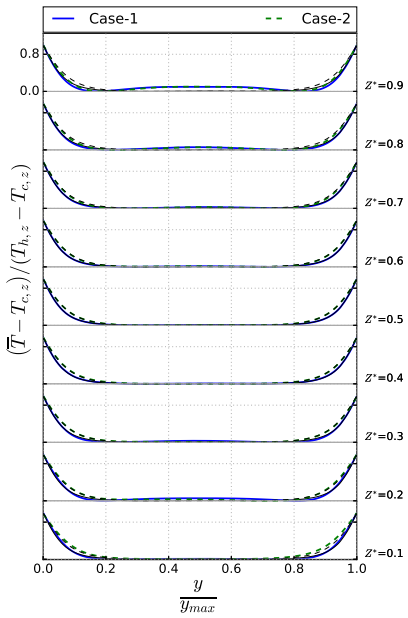

(a) Line_1

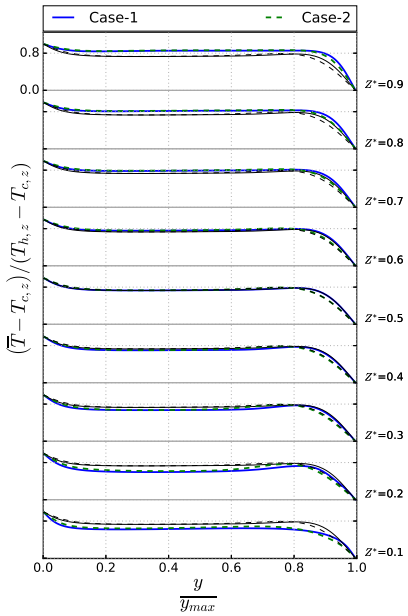

(b) Line_5

Fig. 11: Temperature profiles plotted at differing axial locations. The superimposed black-thin lines are for the profiles taken at mid-height for the cavity. The line styles refer to the pertaining case. The scale for each respective sub-figure is shown in the upper left corner.

bulence remains very low and the flow is laminar until down to around $Z^* = 0.2$, where transition apparently occurs. Below turbulence appears to spread broadly away from the containment wall and into the inner sub-channels.

Figures 4(b&c), 5(a) and 6(a) paint a picture on how the resulting jet flow convects turbulence towards the interior. Due to the cross-flow, the jet would also generate shear turbulence on the rod surface. As the jet flow transverses into the interior it weakens reducing the spread of turbulence. Line_4 (third rank rods) at Z^* = 0.1 has uniform turbulence distribution across the core. This distribution is a result of convected turbulence increasing the free stream turbulence.

Ascending with height, the turbulent kinetic energy profile immediately transitions to a typical shear profile. Lines_1 (rod rank one) and Line_3 (rod rank two), give a further indication of the declining influence of the jet. With increasing distance from the containment wall, turbulence levels in the core reduce along with the peaks becoming more biased towards the rod surface. Development profiles below $Z^* = 0.1$ clearly evidence this (Figure 14). The transition locations appear different, this has also been evidenced in the velocity profiles. Line_1, which is furthest away from the con-

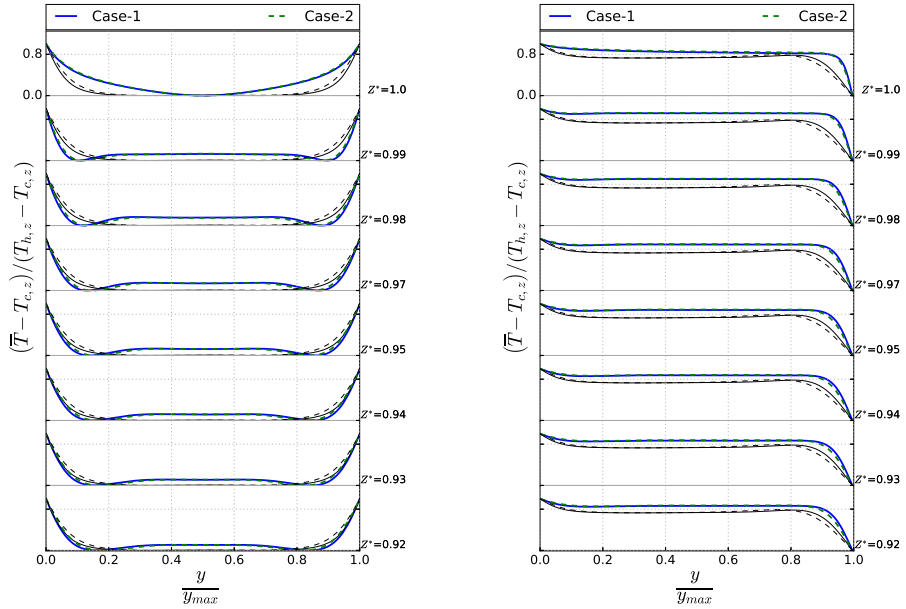

(a) Line_1 - top

(b) Line_5 - top

(c) Line_1 - bottom

(d) Line_5 - bottom

Fig. 12: Temperature profiles plotted near the bottom wall $Z^* = 0.01$ to 0.08 and near the top wall $Z^* = 0.92$ to 1.0. The profiles are normalised using local quantities. The superimposed black-thin lines are for the profiles taken at mid-height for the cavity. Line styles for the mid-height profiles follow that given for the case. The scale for each respective sub-figure is shown in the upper left corner.

tainment transitions at $Z^* \approx 0.33$, while Line_3 transitions earlier at $Z^* \approx 0.2$. Line_4 initially transitions much earlier and remains relatively unchanged between $Z^* = 0.03$ and $Z^* = 0.08$. However, at $Z^* \approx 0.2$ there is another transition to the characteristic turbulence distribution observed at the other rod gap locations further away from the containment wall.

3.3. Laminar boundary layer

3.3.1. Containment wall

Previously explored qualitative data has suggested the containment surface is laminar at the top and the components (rods and containment) behave as if they are isolated. Based on this, it is therefore worth considering for the large diameter containment; how well the LES data compares against a similarity solution for laminar natural convection flow on a vertical flat surface. The similarity solution by Ostrach[24] is used. Momentum and energy are transformed through the introduction of the similarity variable η and stream function Ψ shown in Equation 11.

$$\eta = \frac{y}{z}\left(\frac{\mathrm{Gr}_{z,\Delta T}}{4}\right)^{1/4} \tag{11a}$$

$$\Psi = F(\eta)\left[4v\left(\frac{\mathrm{Gr}_{z,\Delta T}}{4}\right)^{1/4}\right] \tag{11b}$$

The resulting transformed equations are given in Equation 12 for both momentum and energy:

$$F''' + 3FF'' - 2F'^2 + T^* = 0 \tag{12a}$$

$$T^{*\prime\prime} + 3\mathrm{Pr}FT^{*\prime} = 0 \tag{12b}$$

where T^* is the dimensionless temperature, which is defined as $T - T_\infty / T_w - T_\infty$. The set of coupled higher order differential equations are reduced into a set of first order differential equations. A full description of the method used to solve the system of equations is given in the large aspect ratio paper[19]. Results for the similarity solution comparison are presented in Figure 15. As can be seen, even though the containment surface is cylindrical and within a confined domain, there are very good comparisons at the upper sections, where the flow is laminar as earlier suggested.

Ostrach's similarity solution for laminar flow is compared against the LES temperature data extracted for Line_5 and Line_6. Figure 16 shows the results of this comparison. There is fairly good agreement at the top with differences between the laminar solution and LES data increasing as the flow descends.

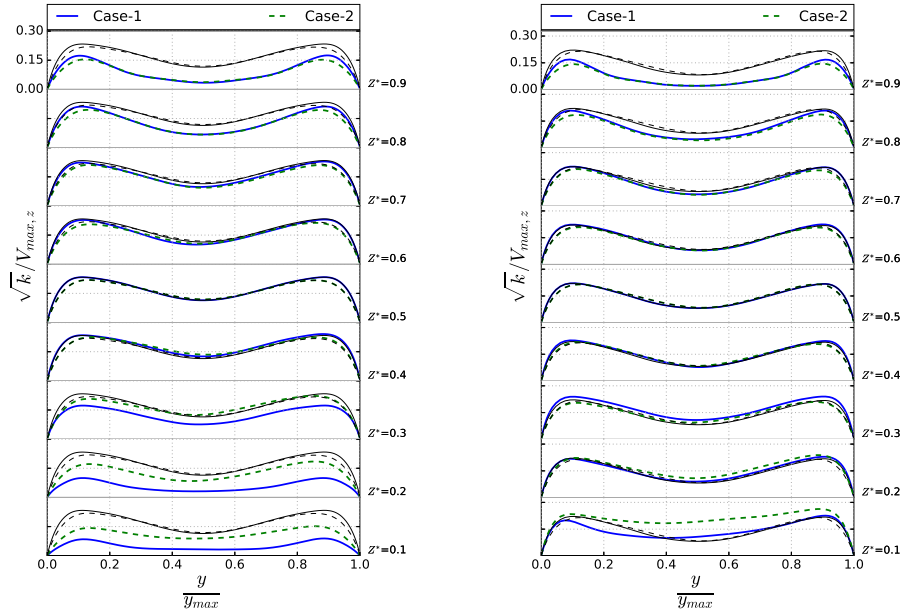

(a) Line_1 (b) Line_3

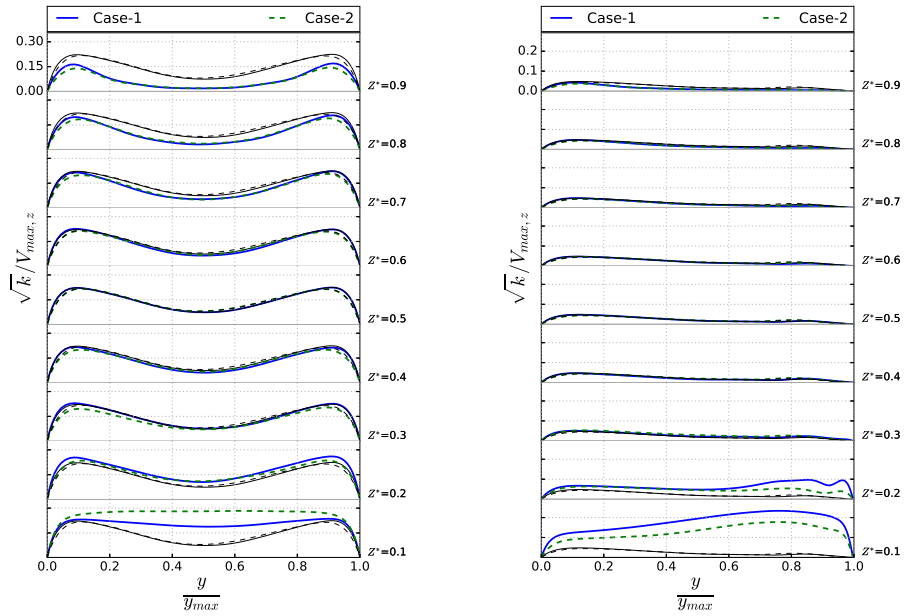

(c) Line_4 (d) Line_5

Fig. 13: Profiles of turbulent kinetic energy plotted at differing axial locations. The maximum velocity $v_{max,z}$ of the profile is used in normalisation. The superimposed black-thin lines are for the profiles taken at mid-height for the cavity. The line styles refer to the pertaining case. The scale for each respective sub-figure is shown in the upper left corner.

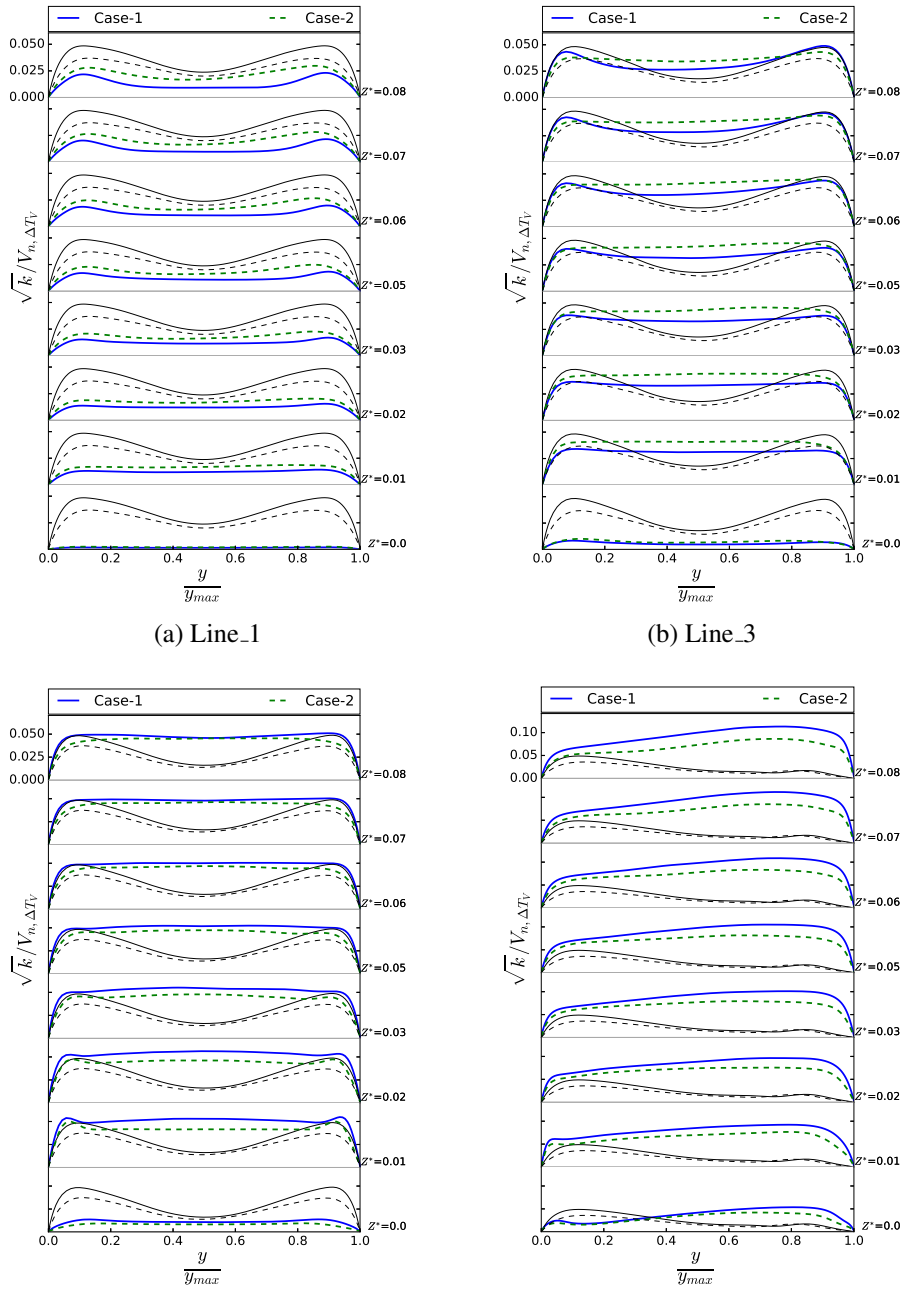

(a) Line_1

(b) Line_3

(c) Line_4

(d) Line_5

Fig. 14: Turbulent kinetic energy profiles plotted near bottom wall upto a height of $Z^* = 0.0$ to 0.08. To normalise the profile the buoyant velocity is used. The superimposed black-thin lines are for the profiles taken at mid-height for the cavity. Line styles for the mid-height profiles are specified according to that of the pertaining case. The scale for each respective sub-figure is shown in the upper left corner.

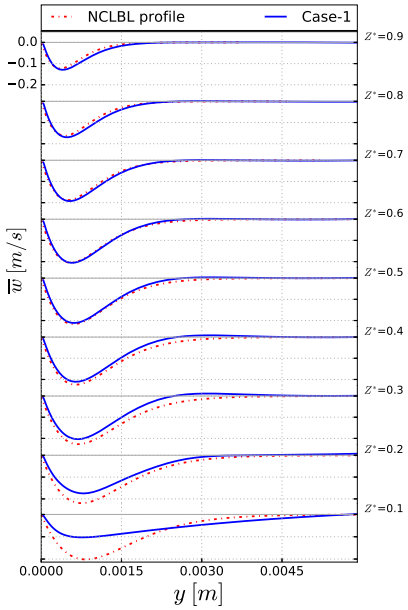

(a) Line_5

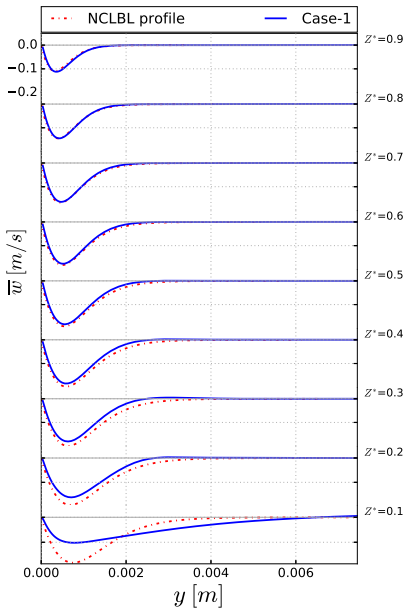

(b) Line_6

Fig. 15: Comparison of LES data from Case-1 against the similarity solution by Ostrach[24]. Data is extracted from the containment surface (now given as $y = 0$) to the stagnant flow region.

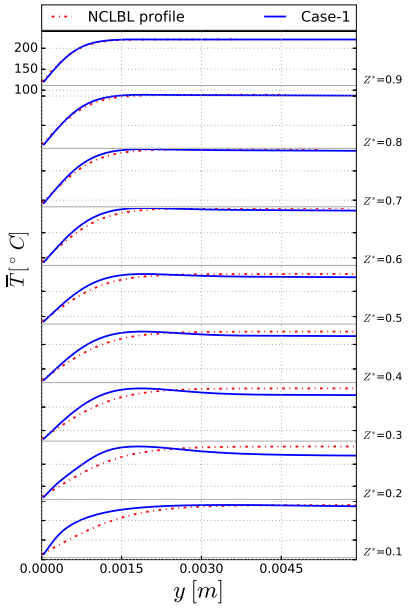

(a) Line_5

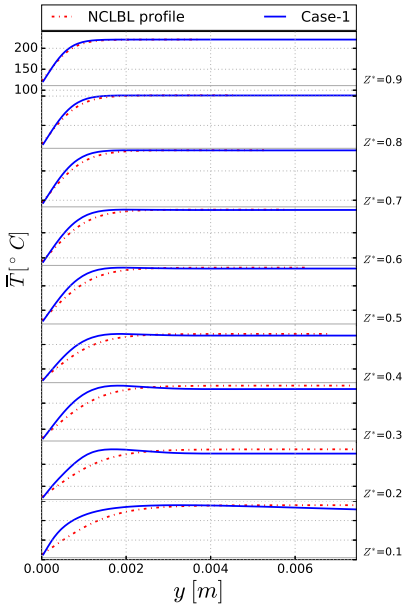

(b) Line_6

Fig. 16: Comparison of LES data from Case-1 against the similarity solution by Ostrach[24] for temperature. Data is extracted from the containment surface now located at $y = 0$.

3.3.2. Rod wall

Profiles extracted across the rod gap at Line_1 are compared against the similarity so-

lution for slender vertical cylinders reported by Popiel[25] but originally published by Sparrow and Gregg[26]. The similarity variable (η) and the radius of curvature effect (ξ) are used to solve the series expression shown in Equation 13. The first term in the series expansion is equivalent to the flat plate solution by Ostrach[24].

$$f(\eta,\xi) = \xi^2\left[f_0(\eta) + \xi f_1(\eta) + \xi^2 f_2(\eta) + \cdots\right] \tag{13a}$$

$$T^*(\eta,\xi) = T_0^*(\eta) + \xi T_1^*(\eta) + \xi^2 T_2^*(\eta) + \cdots \tag{13b}$$

The series expansions are computed up until the second order term. A detailed description of the method used to solve the slender cylinder similarity solution is given in the large aspect ratio paper[19].

Figure 17 compares the data extracted along Line_1 against the similarity solution by Sparrow and Gregg[26]. Below $Z^* = 0.1$ there is good agreement and above this height the extracted data departs from the similarity solution. Velocity profiles have shown for Line_1 at $Z^* = 0.33$ the flow is fully developed. Up until $Z^* = 0.1$, the flow is clearly laminar. Above $Z^* = 0.1$ and below $Z^* = 0.33$ the flow is within the transition regime with transition to turbulence occurring by $Z^* = 0.33$. On the rods it is evident there is natural convection boundary layer forming but with a much reduced development length in comparison to the containment.

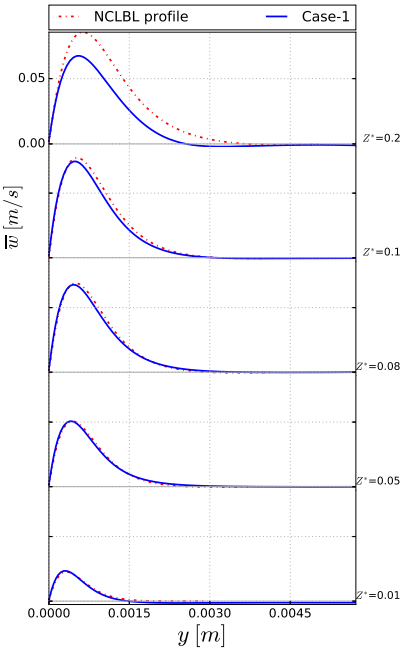

Fig. 17: Comparison of LES data from Case-1 against the similarity solution for cylinders by Sparrow and Gregg[26]. Data is extracted from the cylindrical rod surface at $y = 0$ to the stagnant flow region.

The slender cylinder similarity solution for laminar flow by Sparrow and Gregg[26] is used to compare against the LES temperature data across the rod gap. Results in Figure 18 show good comparisons, at or below $Z^* = 0.1$.

3.4. Sub-channel & bulk variation

In Figure 3, the sub-channel divisions are defined. Using these divisions, the mass flow

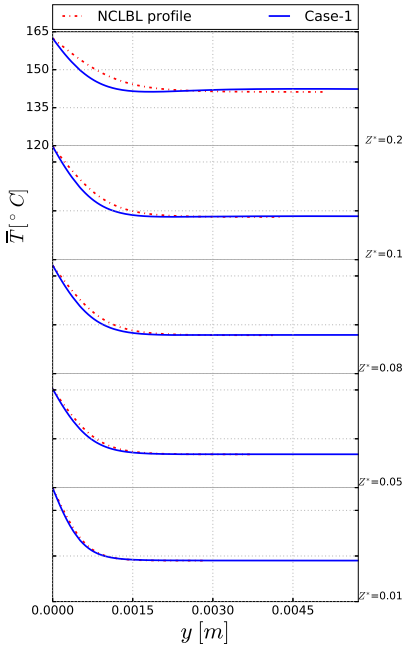

(a) Line_1: $Z^* = 0.01$ to 0.2

Fig. 18: Temperature comparison of LES data from Case-1 against the similarity solution for cylinders by Sparrow and Gregg[26]. Data is extracted from the cylindrical rod surface at $y = 0$ to the stagnant flow region.

This behaviour appears largely driven by the transition to turbulence of the containment surface along with an impingement effect driving the flow towards the interior. Crossflow vectors in Figure 4(b) help illustrate this behaviour.

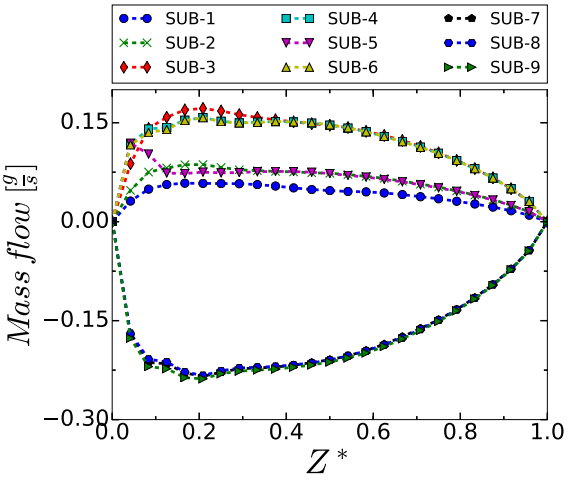

Fig. 19: Sub-channel massflow variation as a function of height.

variation is computed at this level of resolution and presented in Figure 19. Peak mass flow occurs at the square sub-channels and this is largely to be expected as they would have a larger rod perimeter. The flow is constrained to the heated walls with stagnant sub-channels. Sub-channel_5 which is triangular exhibits an interesting distribution. Up to $Z^* \approx 0.05$ the mass flow is equivalent to that of the square sub-channels. Past this height, there is a drastic reduction in the mass flow reducing it to a level equivalent to the other triangular arrays.

The sub-channel variation of the fluid and solid temperature is shown in Figure 20. It is interesting to see that at any axial location, the temperature of all inner sub-channels (1 to 6) are the same and those from the external sub-channels (7 to 9) are also the same but different from the former group. The fuel rod temperatures show no discernible sub-channel variation at any axial location. Both the fluid and fuel rods exhibit a linear temperature gradient away from the domain ends. In simple cavities, this has also been observed by various

investigators[2, 6].

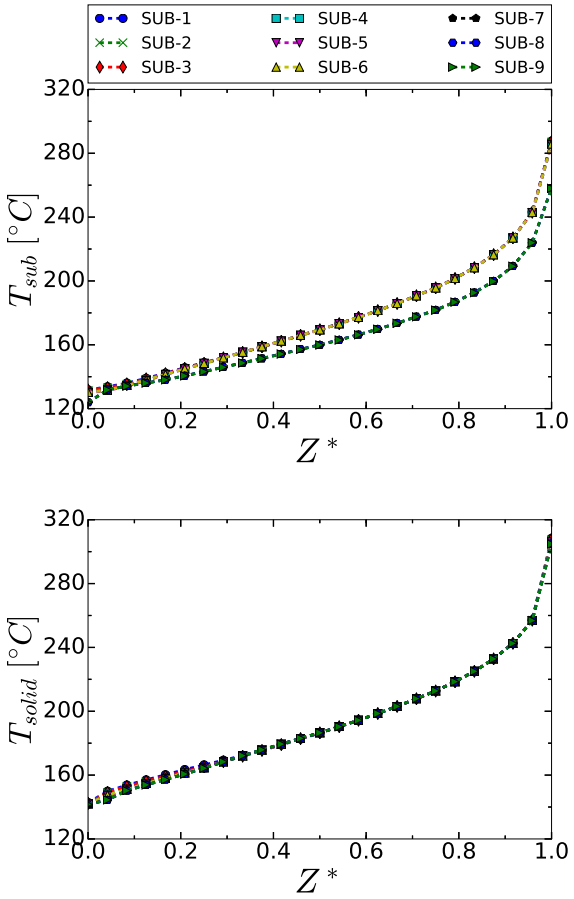

Fig. 20: Sub-channel temperature variation as a function of height.

3.5. Correlations

Heat transfer correlations are presented for the containment surface, rod surfaces and the sub-channels. The Fanning friction factor computed at the containment surface is also reported. Figure 21(a) presents the Nusselt number at the containment surface. The Rayleigh number is computed using the local temperature difference and the length scale is the distance from the top of the domain. Equation 14 is used to calculate the local Nusselt number. The average Nusselt number is then obtained by averaging along the containment surface per axial location in the circumferential direction.

$$\mathrm{Nu} = \frac{q'' \cdot z}{(T_w - T)\,\lambda} \tag{14}$$

The Nusselt number profiles show a linear increase with Rayleigh number, up until $\mathrm{Ra}_{z,\Delta T} \approx 2 \times 10^9$ and 6×10^9 for the lowest heating cases and highest heating case, respectively. Afterwards, there is a sudden jump in Nusselt number indicating turbulence transition. Correlating the LES data for the Laminar portion yields $0.43\mathrm{Ra}_{z,\Delta T}^{0.26}$. Assuming a flat vertical plate, the laminar correlation for Nusselt number has an exponent of 0.25. This shows a remarkable similarity between this geometry (for flow at the containment surface) and an unconfirmed vertical surface, further showing the underlying physics can be considered somewhat the same.

Next, the Fanning friction factor for the containment surface is presented in Figure 21(b) as a function of Rayleigh number. To compute, the fanning factor the peak axial velocity is used. Similar to the Nusselt plot, an initial

laminar region is seen with a transition region occurring at higher Rayleigh numbers.

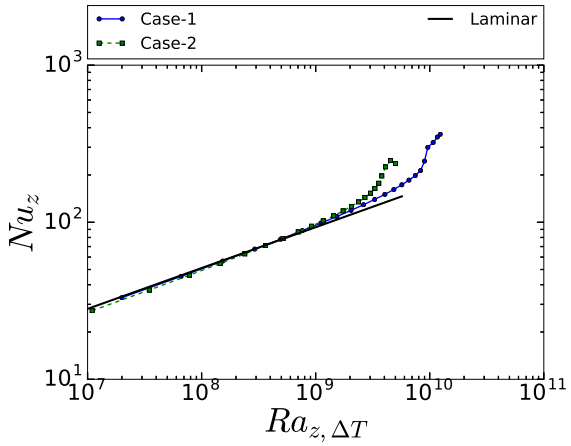

(a) Nusselt number

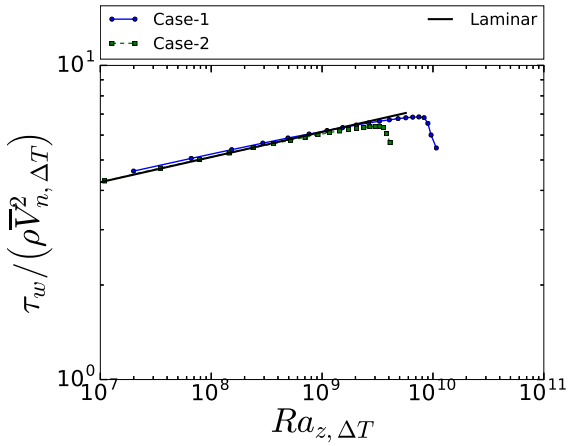

(b) Fanning friction factor

Fig. 21: Variation of Nusselt and Fanning friction factor as a function of Rayleigh.

The Nusselt number on the fuel rods has also been calculated. To relate the derived correlation to those obtained for rectangular cavities, a mirror profile approach is adopted. This approach was proposed by Trinca[27] in earlier preliminary work and Figure 22 illustrates this. In rectangular cavities, the dimensionless

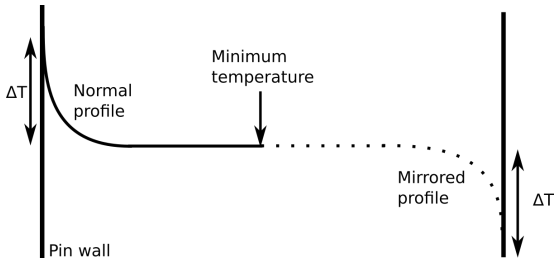

Fig. 22: Illustration of the mirror profile approach used to relate computed Nusselt values to rectangular cavities.

variables are computed using the temperature difference between the hot and cold wall. Using the mirror profile approach the following equivalent definitions are used:

$$\mathrm{Nu} = \frac{q''\mathrm{L}}{2\Delta T\lambda} \tag{15a}$$

$$\mathrm{Ra} = \frac{g\beta L^3\left(2\Delta T\right)}{\alpha v} \tag{15b}$$

where ΔT is the difference between the wall and minimum temperature. The characteristic length scale used L is defined as the rod gap spacing.

Results obtained from this approach are presented in Figure 23. The aspect ratio, defined as H/L where H is the height and L is the rod gap length, ranges from 14 to 26. Data from the LES simulation is extracted between $Z^* = 0.3$ and 0.7, as the flow at the top and bottom is known to be laminar.

Heat transfer correlations for rectangular

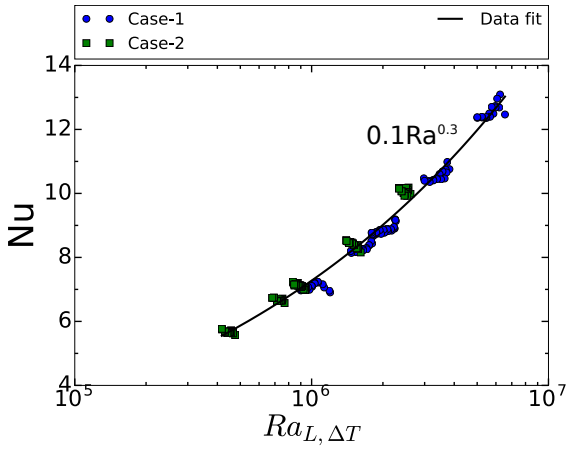

(a) Without aspect ratio scaling.

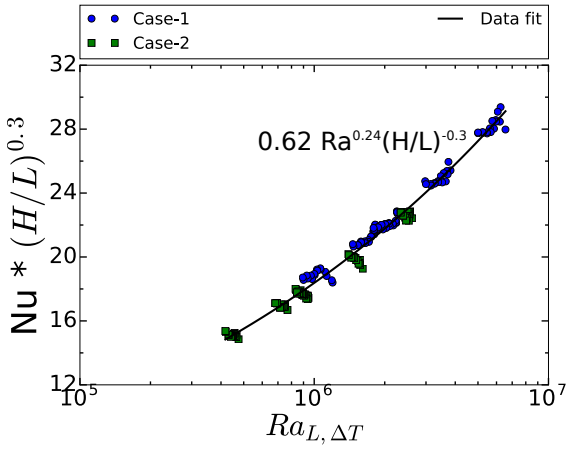

(b) With aspect ratio scaling.

Fig. 23: Nusselt values computed across the rodgap using the mirror profile approach. Correlation for sub-figure (a) is Data fit = $0.1\mathrm{Ra}_{L,\Delta T}^{0.3}$ and for sub-figure (b) is Data fit = $0.62\mathrm{Ra}_{L,\Delta T}^{0.24}\,(H/L)^{-0.3}$.

cavities obtained by Macgregor and Emery[3] are given below with and without Nusselt scaling by the aspect ratio:

$$\mathrm{Nu} = 0.046\mathrm{Ra}_{L,\Delta T}^{0.333} \tag{16a}$$

$$\mathrm{Nu} = 0.42\mathrm{Ra}_{L,\Delta T}^{0.25}\mathrm{Pr}^{0.012}\,(H/L)^{-0.3} \tag{16b}$$

Equation 16(a) is valid for aspect ratios up to 40 with a Rayleigh number range of 10^6 to 10^9. Equation 16(b) is valid for Rayleigh numbers 10^4 to 10^7 and aspect ratios up to 40.

The LES derived data correlations are $0.1\mathrm{Ra}_{L,\Delta T}^{0.3}$ and $0.62\mathrm{Ra}_{L,\Delta T}^{0.24}\,(H/L)^{-0.3}$ comparing to the forms proposed by Macregor and Emery[3], respectively. It can be noted the exponents are very similar, even though there is a significant difference in the geometry. Similarly, the correlations from Keyhani et al. [12] had exponents of 0.323 and 0.332 for the differing rod bundle configurations. In general, Nusselt number values for turbulent flow are known to follow the relation $C\mathrm{Ra}^{0.33}$ for rectangular cavities and flat vertical surfaces. For the more complex geometry and conditions investigated herein, this dependence has been shown to still hold, which is a remarkable result.

In a precursor simulation to those presented herein by Trinca[27] an unstructured grid was used to simulate a short geometry bundle. A single heating case of 325 W/m^2 at a pressure of 4 Mpa was investigated. Using the mirror profile approach, the correlations obtained were $0.095\mathrm{Ra}_{L,\Delta T}^{0.32}$ and $1.081\mathrm{Ra}_{L,\Delta T}^{0.22}\,(H/L)^{-0.3}$. The obtained corre-

lations are similar to those from the updated simulations.

4. Conclusion

LES simulations have been conducted for a sealed short rod bundle. The flow and temperature distributions observed are akin to the boundary layer flow regime[2, 3]: Flow occurs in the boundary layers and the core is largely stagnant with a uniform stratified temperature field. The formation and development of momentum and thermal boundary layer on the rods and containment wall are important feature of the flow system.

Flow at the containment surface gradually develops from laminar and transitions to turbulence occurs close to the bottom-end. After the point of transition, turbulence generated here is spread to the interior sub-channels by the ensuing jet flow. The spread of turbulence is demonstrated to affect boundary layer development on the rods. The rod ranks closest to the containment wall are shown to transition faster. While rods in the first rank, which is furthest from the containment are largely unaffected and transition to turbulence later. Using the Q-criterion, turbulence structures are evidenced within the vicinity of the fuel rod surfaces and lower half of the containment wall.

Correlations extracted for the rod surfaces using a mirror profile approach have shown the Nusselt number has a Rayleigh dependence of $\mathrm{Nu} = 0.1\mathrm{Ra}^{0.3}$, which is similar to that for a rectangular cavity. Nusselt number and friction factor correlations at the containment wall confirm transition occurs close to the bottom-end. The formation of a fully turbulent core as seen by other investigators such as Elder[1] and Betts and Bokhari[4] has not been observed in this short geometry. Thus it is likely if a larger domain is modelled the flow and heat transfer characteristics would be appreciably altered.

Acknowledgements

This work is supported through a studentship provided by EDF energy and has been performed using resources provided by the Cambridge Tier-2 system funded by EPSRC Tier-2 capital grant EP/P020259/1.

Appendix

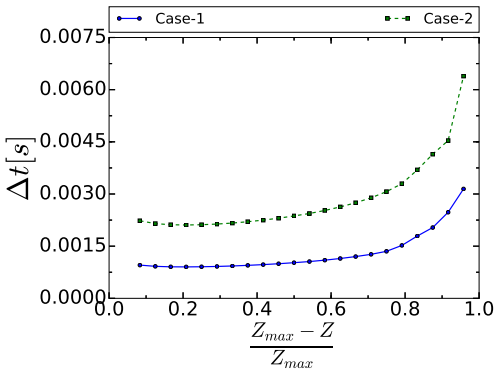

Fig. A1: Profiles of the wall time step along the containment wall generated for case-1 and case-2. The 0 location is the top of the containment wall.

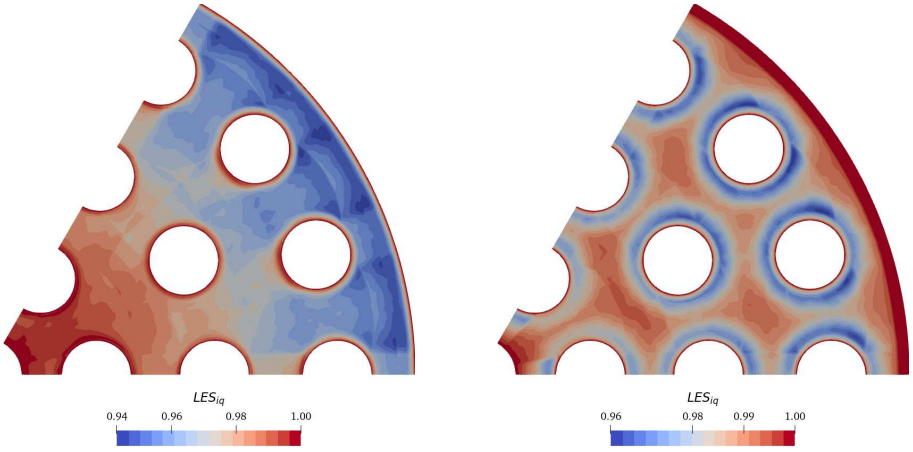

(a) $Z^* = 0.04$ (b) $Z^* = 0.5$

Fig. A2: Contours of the LES_IQ$_v$ parameter at varying heights and taken from Case-1. The scalebar is reset at each axial location to maximise the variation. LES is considered to be good if the values obtained are LES_IQ$_v > 0.8$.

References

[1] J. W. Elder, Laminar free convection in a vertical slot, Journal of Fluid Mechanics 23 (1) (1965) 77–98. doi:10.1017/S0022112065001246.

[2] J. W. Elder, Turbulent free convection in a vertical slot, Journal of Fluid Mechanics 23 (1) (1965) 99–111. doi:10.1017/S0022112065001246.

[3] R. K. MacGregor, A. F. Emery, Free Convection Through Vertical Plane Layers—Moderate and High Prandtl Number Fluids, Journal of Heat Transfer 91 (3) (1969) 391–401. doi:10.1115/1.3580194.

[4] P. Betts, I. Bokhari, Experiments on turbulent natural convection in an enclosed tall cavity, International Journal of Heat and Fluid Flow 21 (6) (2000) 675–683. doi:10.1016/S0142-727X(00)00033-3. URL https://www.sciencedirect.com/science/article/pii/S0142727X00000333

[5] W. M. Lewandowski, M. Ryms, H. Denda,

Natural convection in symmetrically heated vertical channels, International Journal of Thermal Sciences 134 (2018) 530–540. doi:10.1016/J.IJTHERMALSCI.2018.08.036.
URL https://www.sciencedirect.com/science/article/pii/S1290072917317453

[6] S. Kimura, A. Bejan, The boundary layer natural convection regime in a rectangular cavity with uniform heat flux from the side, Journal of Heat Transfer 106 (1) (1984) 98–103. doi:10.1115/1.3246666.

[7] S. Paolucci, D. R. Chenoweth, Transition to chaos in a differentially heated vertical cavity, Journal of Fluid Mechanics 201 (1989) 379–410.

[8] K. Nakao, Y. Hattori, H. Suto, Numerical investigation of a spatially developing turbulent natural convection boundary layer along a vertical heated plate, International Journal of Heat and Fluid Flow 63 (2017) 128–138. doi:10.1016/J.IJHEATFLUIDFLOW.2016.09.006.
URL https://www.sciencedirect.com/science/article/pii/S0142727X16305501

[9] T. Versteegh, F. Nieuwstadt, Turbulent budgets of natural convection in an infinite, differentially heated, vertical channel, International Journal of Heat and Fluid Flow 19 (2) (1998) 135–149. doi:10.1016/S0142-727X(97)10018-2.
URL https://www.sciencedirect.com/science/article/pii/S0142727X97100182

[10] S. Paolucci, Direct numerical simulation of two-dimensional turbulent natural convection in an enclosed cavity, Journal of Fluid Mechanics 215 (1990) 229–262. doi:10.1017/S0022112090002634.

[11] S. S. Goodrich, W. R. Marcum, Natural convection heat transfer and boundary layer transition for vertical heated cylinders, Experimental Thermal and Fluid Science 105 (2019) 367–380. doi:10.1016/J.EXPTHERMFLUSCI.2019.04.010.
URL https://www.sciencedirect.com/science/article/pii/S0894177718315528{#}f0005

[12] M. Keyhani, F. A. Kulacki, R. N. Christensen, Experimental investigation of free convection in a vertical rod bundle—a general correlation for nusselt numbers, Journal of Heat Transfer 107 (3) (1985) 611–623. doi:10.1115/1.3247468.

[13] M. Keyhani, T. Dalton, Natural convection heat transfer in horizontal rod-bundle enclosures, Journal of Heat Transfer 118 (3) (1996) 598–605. doi:10.1115/1.2822674.

[14] X. D. Mao, H. Xia, Natural Convection Heat Transfer of the Horizontal Rod-Bundle in a Semi-closed Rectangular Cavity, Frontiers in Energy Research 8 (May) (2020) 1–7. doi:10.3389/fenrg.2020.00074.

[15] Y. G. Park, M. Y. Ha, J. Park, Natural convection in a square enclosure with four circular cylinders positioned at different rectangular locations, International Journal of Heat and Mass Transfer 81 (2015) 490–511. doi:10.1016/j.ijheatmasstransfer.2014.10.065.

[16] M. Arshad, M. H. Inayat, I. R. Chughtai, Experimental study of natural convection heat transfer from an enclosed assembly of thin vertical cylinders, Applied Thermal Engineering 31 (1) (2011) 20–27. doi:10.1016/j.applthermaleng.2010.07.031.

[17] A. J. N. Khalifa, Z. A. Hussien, Natural convection heat transfer from a single and multiple heated thin cylinders in water, Heat Mass Transfer 51 (11) (2015) 1579–1586. doi:10.1007/s00231-015-1524-4.
URL http://dx.doi.org/10.1007/s00231-015-1524-4

[18] Y. F. Rao, E. K. Glakpe, Three-dimensional natural convection in an enclosed vertical rod bundle with mixed boundary conditions, International Journal of Heat and Mass Transfer 36 (6) (1993) 1517–1528. doi:10.1016/S0017-9310(05)80062-6.

[19] K. Chinembiri, S. He, J. Li, Natural circulation in a sealed rod bundle of large aspect ratio, Applied Thermal Engineering, (188). doi:https://doi.org/10.1016/j.applthermaleng.2020.116534.

[20] EDF R&D, Code Saturne 4.0.0 Theory Guide, Tech. rep., EDF (2015).

[21] F. Nicoud, F. Ducros, Subgrid-scale stress modelling based on the square of the velocity, Agricultural Economics Research Review 19 (2006) 37–48. arXiv:arXiv:1503.01439v1, doi:10.1016/j.jcp.2004.10.018.

[22] E. Lemmon, M. Huber, M. McLinden, NIST Standard Reference Database 23: Reference Fluid Thermodynamic and Transport Properties (REFPROP), Version 9.0. (2010).

[23] I. B. Celik, Z. N. Cehreli, I. Yavuz, Index of resolution quality for large eddy simulations, Journal of Fluids Engineering, Transactions of the ASME 127 (5) (2005) 949–958. doi:10.1115/1.1990201.

[24] S. Ostrach, An analysis of laminar free-convection flow and heat transfer about a flat plate parallel to the direction of the generating body force, Tech. rep., National Advisory Committee for Aeronautics, Cleveland (1952). arXiv:arXiv:1011.1669v3, doi:10.1017/CBO9781107415324.004.

[25] C. O. Popiel, Free convection heat transfer from vertical slender cylinders: A review, Heat Transfer Engineering 29 (6) (2008) 521–536. doi:10.1080/01457630801891557.

[26] E. Sparrow, J. Gregg, Laminar free convection from a vertical plate with uniform surface heat flux, in: ASME 78, 1956, pp. 435 – 440.

[27] C. Trinca, Nuclear Fuel Route Thermal Hydraulics Analysis for Advanced Gas-cooled Reactors (AGRs), Thesis, University of Sheffield, Sheffield (2019).